Research Article Vol. 40, No. 7 / July 2023 / Journal of the Optical Society of America B 1857

Journal of the Optical Society of America B

OPTICAL PHYSICS

Inverse design of functional photonic patches by adjoint optimization coupled to the generalized Mie theory

Yilin Zhu,[1] Yuyao Chen,[2] Sean Gorsky,[2] Tornike Shubitidze,[2] and Luca Dal Negro[1,2,3,*]

[1]Division of Material Science and Engineering, Boston University, 15 Saint Mary's Street, Brookline, Massachusetts 02446, USA
[2]Department of Electrical & Computer Engineering and Photonics Center, Boston University, 8 Saint Mary's Street, Boston, Massachusetts 02215, USA
[3]Department of Physics, Boston University, 590 Commonwealth Avenue, Boston, Massachusetts 02215, USA
*dalnegro@bu.edu

Received 29 March 2023; revised 29 May 2023; accepted 30 May 2023; posted 31 May 2023; published 28 June 2023

We propose a rigorous approach for the inverse design of functional photonic structures by coupling the adjoint optimization method and the 2D generalized Mie theory (2D-GMT) for the multiple scattering problem of finite-sized arrays of dielectric nanocylinders optimized to display desired functions. We refer to these functional scattering structures as "photonic patches." We briefly introduce the formalism of 2D-GMT and the critical steps necessary to implement the adjoint optimization algorithm to photonic patches with designed radiation properties. In particular, we showcase several examples of periodic and aperiodic photonic patches with optimal nanocylinder radii and arrangements for radiation shaping, wavefront focusing in the Fresnel zone, and for the enhancement of the local density of states (LDOS) at multiple wavelengths over micron-sized areas. Moreover, we systematically compare the performances of periodic and aperiodic patches with different sizes and find that optimized aperiodic Vogel spiral geometries feature significant advantages in achromatic focusing compared to their periodic counterparts. Our results show that adjoint optimization coupled to 2D-GMT is a robust methodology for the inverse design of compact photonic devices that operate in the multiple scattering regime with optimal desired functionalities. Without the need for spatial meshing, our approach provides efficient solutions at a strongly reduced computational burden compared to standard numerical optimization techniques and suggests compact device geometries for on-chip photonics and metamaterials technologies.

https://doi.org/10.1364/JOSAB.491882

Inverse design is an important methodology for the nanophotonics community that enables the development and prototyping of novel devices with desired characteristics and functionalities, greatly enriching the photonic design library beyond standard templates [1]. In a typical inverse design situation, an objective function for the system is first designed and then search algorithms are applied to vary the system's design parameters and optimize an objective function value until it reaches a desired threshold. Gradient-based search algorithms are commonly used that iteratively evaluate the gradient of the objective function with respect to the design parameters and then update these parameters using the gradient information [1,2]. The adjoint optimization method is a rigorous and general approach that has been widely used for the inverse design of photonic devices, such as parametrized metasurfaces [3–5], on-chip demultiplexer waveguides [6,7], and nonlinear optical switches [8]. The calculation of gradients in forward simulations is typically performed by numerical methods, such as the finite-element method (FEM) and finite-difference-time-domain (FDTD) [3,4,6–8]. However, standard numerical methods are computationally expensive because they require spatial meshing [9]. Therefore, if one could obtain the gradients of the desired system's parameters in analytical or semi-analytical closed forms, then very efficient adjoint optimizations would be achieved based only on one single forward simulation. Recent examples of analytical gradient calculations include the inverse design of metasurfaces using the coupled-mode theory (CMT) [10], and the optimization of compact optical elements based on spherical nanoparticles using the multisphere generalized Mie theory (3D-GMT) approach [11,12]. Latest techniques also leverage the concept of automatic differentiation (AD) used in artificial neural networks for the inverse design of meta-optics [13,14].

In this paper, we introduce and use the adjoint optimization approach coupled to 2D generalized Mie theory (2D-GMT),

which rigorously solves Maxwell's equations for 2D geometries of arbitrary arrays of scattering cylinders. Using this powerful tool, we demonstrate the inverse design of "photonic patches," which are finite-sized arrays of nanocylinders with positions and radii efficiently optimized to achieve desired functionalities over small-footprint areas. We remark that rigorous simulations of scattering systems based on 2D-GMT enable the engineering of 3D photonic crystal membranes where the out-of-plane losses, which originate from finite height of the devices along the z direction, are considered within the effective refractive index method [15]. In this approximation, which is satisfied for low refractive index contrast, the material dispersion of the dielectric medium is replaced by the effective index of the fundamental guided mode in the unperturbed (without air holes) 3D heterostructure, enabling direct design of resonant devices based on the silicon nitride materials platform [16–20]. We would like to emphasize that the adjoint optimization method, like any other gradient-based optimization algorithm that tackles high-dimensional nonconvex problems, does not guarantee the convergence to a global optimal solution. Nevertheless, using this approach it is still possible to identify largely improved device geometries that perform remarkably well and are superior to the traditional photonic designs [1,21].

Our paper begins with an overview in the first section of the 2D-GMT formalism that solves the multiple scattering problem for nonoverlapping nanocylinders under an excitation wave perpendicular to the axis of the cylinders. In particular, we discuss analytical closed-form expressions for the far-field scattering intensity and the local density of states (LDOS) that enable the efficient implementation of the adjoint optimization algorithm. Detailed results on the analytical calculations of gradient terms are also provided. Using these results, we provide several application examples of designed photonic patches optimized to perform multiwavelength radiation shaping, near-field focusing, and to enhance the LDOS over small device areas. Our results demonstrate that the inverse design of photonic patches provides complex optical functionalities over significantly reduced areas compared to traditional photonic crystals and enables scalability advantages for the optical integration of aperiodic structures [22,23].

1. OVERVIEW OF 2D-GMT

In this section, we provide a brief overview of the 2D-GMT formalism by introducing the transfer matrix equation, the scattered far-field amplitude and the local density of states (LDOS). Particular emphasis is placed on closed-form analytical results that enable the efficient calculation of the gradient terms. A detailed derivation and implementation of the 2D-GMT for the nanocylinder array can be found in references [9,24].

A. Derivation of the Transfer Matrix Equation

The essential idea of 2D-GMT is to expand the fields into a sum of cylindrical Bessel and Hankel functions, which form a complete basis in the 2D domain. Using Graf's addition theorem, we then enforce the electromagnetic boundary conditions at the surface of each cylinder and obtain a matrix equation that relates the known expansion coefficients of the excitation source with the unknown expansion the coefficients of the internal and scattered fields. Therefore, the solution of the scattering problem is conveniently formulated as a matrix inversion problem for the unknown field expansion coefficients, as detailed below.

A typical geometry for which the 2D-GMT solves the scattering problem is displayed in Fig. 1. In particular, it consists of an aggregate of cylinders with positions (x_n, y_n) and radii r_n with complex relative permittivities ϵ_n and permeabilities μ_n. The system is embedded in a nonabsorbing dielectric host medium with real permittivity ϵ_o and permeability μ_o. As we restrict the wave propagation to in-plane directions only, the field solutions can be represented as TM polarization, where the electric field $\mathbf{E} = E_z\hat{\mathbf{z}}$ is oriented along the axis of the cylinders (z axis), or TE polarization, where $\mathbf{H} = H_z\hat{\mathbf{z}}$ is oriented along the z axis. In our discussion, we denote the relevant field component along the cylindrical axis as $\varphi(\mathbf{r})$, standing either for E_z or for H_z, depending on the polarization considered. In the schematic shown in Fig. 1, the exterior field φ^E, which exists only outside nanocylinders, consists of the sum of the incident field $\varphi^{E,\text{inc}}$ and the scattered field $\varphi^{E,\text{sca}}$. These contributions are expanded as an infinite sum of complete basis functions for the cylindrical geometry, which are the cylindrical Bessel and the Hankel functions. Therefore, we represent the exterior field as

$$\varphi^E(\mathbf{r}) = \varphi^{E,\text{sca}}(\mathbf{r}) + \varphi^{E,\text{inc}}(\mathbf{r}), \tag{1}$$

$$\varphi^{E,\text{inc}}(\mathbf{r}) = p_z \sum_{\ell=-\infty}^{\infty} a_{n\ell}^{0E} J_\ell(k_o\rho_n) e^{j\ell\theta_n}, \tag{2}$$

$$\varphi^{E,\text{sca}}(\mathbf{r}) = p_z \sum_{n=1}^{N} \sum_{\ell=-\infty}^{\infty} b_{n\ell} H_\ell(k_o\rho_n) e^{j\ell\theta_n}, \tag{3}$$

where $J_\ell(z)$ and $H_\ell(z)$ are Bessel and Hankel functions of the first kind, $k_o = 2\pi\sqrt{\epsilon_o\mu_o}/\lambda$ is the wavenumber in the host medium, ℓ is the angular order of the cylindrical functions, $\mathbf{r}$ is a global position vector, and (ρ_n, θ_n) is the local polar coordinate system with its origin located at the center of the nth ($n = 1, 2, \ldots, N$) cylinder, as shown in Fig. 2(a). The Mie–Lorenz coefficients $a_{n\ell}^{0E}$ depend on the excitation conditions while the coefficients $b_{n\ell}$ are associated to the scattered fields. These quantities are introduced in the local reference frame centered on the nth nanocylinder. The coefficient p_z is used above to ensure that source properties, such as incident intensity or power, appear to be independent of the polarization. Here, we have $p_z = 1/Z_0$ for TE-polarized excitation and $p_z = 1$ for TM-polarized excitation, where Z_0 is the impedance of the host medium.

Similarly, the interior field within the nth nanocylinder φ_n^I has a contribution originating from the sum of the fields scattered from surfaces of all the other cylinders $\varphi_n^{I,\text{sca}}$, not to be confused with the exterior scattered field $\varphi^{E,\text{sca}}$, and one from any source that is present inside the nth cylinder $\varphi_n^{I,\text{sca}}$, so

$$\varphi_n^I(\mathbf{r}) = \varphi_n^{I,\text{src}}(\mathbf{r}) + \varphi_n^{I,\text{sca}}(\mathbf{r}), \tag{4}$$

$$\varphi_n^{I,\text{src}}(\mathbf{r}) = p_z \sum_{\ell=-\infty}^{\infty} a_{n\ell}^{0I} H_\ell(k_n\rho_n) e^{j\ell\theta_n}, \tag{5}$$

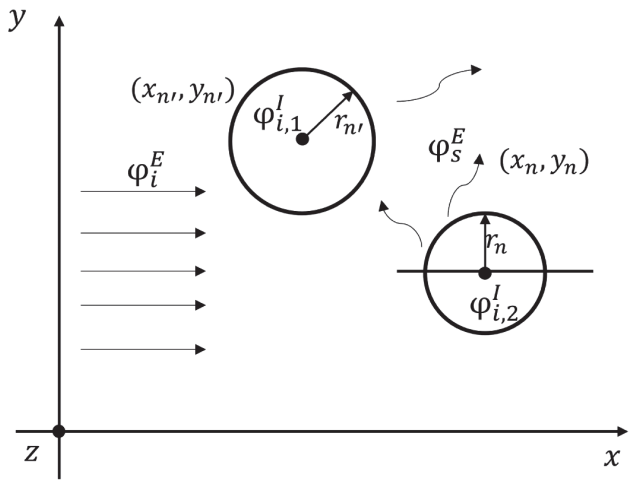

Fig. 1. Schematic of the geometry of the scattering problem for two nanocylinders introducing the relevant notation of 2D-GMT.

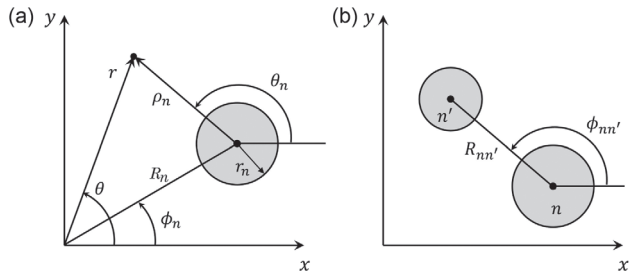

Fig. 2. (a) Schematics of the polar coordinates (r, θ) with origin at (0, 0) and polar coordinates (ρ_n, θ_n) with origin located at the center of the nth cylinder (x_n, y_n). (b) Illustration of the relation between two local frames used in the derivation of Eq. (8).

$$\varphi_n^{I,\mathrm{sca}}(\mathbf{r}) = p_z \sum_{\ell=-\infty}^{\infty} c_{n\ell} J_\ell(k_n \rho_n) e^{j\ell\theta_n}, \tag{6}$$

where $k_n = 2\pi\sqrt{\epsilon_n \mu_n}/\lambda$ is the wavenumber inside the nth cylinder. In the expressions above the coefficients $a_{n\ell}^{0I}$ are related to the known source inside the nth cylinder, if present.

Based on Eqs. (1)–(6), the goal of field calculation is to solve for the unknown coefficients $c_{n\ell}$ and $b_{n\ell}$ given the known coefficients $a_{n\ell}^{0E}$, $a_{n\ell}^{0I}$, through the application of the boundary conditions on the surface of each cylinder. This can be achieved based on the expansion of the exterior field $\varphi^E(\mathbf{r})$ in terms of Bessel and Hankel functions centered only on the nth cylinder by

$$\varphi_n^E(\mathbf{r}) = p_z \sum_{\ell} \left[a_{n\ell} J_\ell(k_o \rho_n) + b_{n\ell} H_\ell(k_o \rho_n)\right] e^{j\ell\theta_n}. \tag{7}$$

Note that Eq. (7) is derived by applying Graf's addition theorem that enables the transformation of cylindrical basis functions from the reference frame of the cylinder n' to that of the cylinder n [9,24,25]. The coefficients $a_{n\ell}$ are expressed as

$$a_{n\ell} = a_{n\ell}^{0E} + \sum_{n'\neq n} \sum_{\ell'=-\infty}^{\infty} e^{j(\ell'-\ell)\phi_{nn'}} H_{\ell-\ell'}\left(k_o R_{nn'}\right) b_{n'\ell'}, \tag{8}$$

where $(R_{nn'}, \phi_{nn'})$ are the polar coordinates of the center of the n'th cylinder with respect to the frame of reference centered on the nth cylinder, as shown in Fig. 2(b). We can now apply the electromagnetic boundary conditions on the surface of each cylinder $\rho_n = r_n$ according to

$$\varphi_n^I(r_n) = \varphi_n^E(r_n)$$

$$\varsigma_n \left.\frac{\partial \varphi_n^I}{\partial \rho_n}\right|_{r_n} = \varsigma_o \left.\frac{\partial \varphi_n^E}{\partial \rho_n}\right|_{r_n}, \tag{9}$$

where $\varsigma_n = 1/\mu_n[1/\epsilon_n]$ and $\varsigma_o = 1/\mu_o[1/\epsilon_o]$ for TM[TE] polarization, respectively. Applying the boundary conditions using Eqs. (4) and (7) and assuming no internal sources inside the scatterers ($a_{n\ell}^{0I} = 0$) we can obtain

$$b_{n\ell} = a_{n\ell} s_{n\ell}, \tag{10}$$

where

$$s_{n\ell} = -\frac{J'_\ell(k_o r_n) - \Gamma_{n\ell} J_\ell(k_o r_n)}{H'_\ell(k_o r_n) - \Gamma_{n\ell} H_\ell(k_o r_n)},$$

$$\Gamma_{n\ell} = \frac{\xi_n k_n J'_\ell(k_n r_n)}{k_o J_\ell(k_n r_n)},$$

$$\xi_n = \frac{\mu_o}{\mu_n}\left[\frac{\epsilon_o}{\epsilon_n}\right] \quad \text{for TM[TE]}. \tag{11}$$

Here, the prime symbol denotes the first derivative of the corresponding function with respect to its entire argument. Substituting Eq. (8) into Eq. (10) yields the relation between $b_{n\ell}$ and $a_{n\ell}^{0E}$ as

$$b_{n\ell} - s_{n\ell} \sum_{n'\neq n} \sum_{\ell'=-\infty}^{\infty} e^{j(\ell'-\ell)\phi_{nn'}} H_{\ell-\ell'}(k_o R_{nn'})\, b_{n'\ell'} = s_{n\ell} a_{n\ell}^{0E}. \tag{12}$$

Such a relation can be written in matrix form as

$$\mathbf{T}\mathbf{b} = \mathbf{a}^0, \tag{13}$$

where we have introduced the transfer matrix or T matrix with elements

$$\mathbf{T}_{nn'}^{\ell\ell'} = \delta_{nn'}\delta_{\ell\ell'} - (1-\delta_{nn'})\, e^{j(\ell'-\ell)\phi_{nn'}} H_{\ell-\ell'}(k_o R_{nn'})\, s_{n\ell}. \tag{14}$$

Here, δ is the Kronecker function and we introduced the vector notation

$$\mathbf{a}^0 = \{a_{n\ell}\} = \left\{s_{n\ell} a_{n\ell}^{0E}\right\}, \quad \mathbf{b} = \{b_{n\ell}\}. \tag{15}$$

In practical implementations, we must limit the range of ℓ in the angular expansions to a specified cutoff order and consider terms ranging from $-\ell_{\max}$ to $\ell_{\max}$. A larger $\ell_{\max}$ value guarantees a more accurate solution but adds computational cost to the numerical solution of the scattering problem. There is a common prescription for choosing $\ell_{\max}$ in generic array geometries, which is $\ell_{\max} \sim 3kr_{\max}$ [9,26,27], where $r_{\max}$ is the radius of the largest cylinder in the array. However, a more reliable method is to perform convergence analysis directly by comparing results obtained for different choices of ℓ until no variations in the solutions occur for the specific geometry under study. This is the

approach that we used in the optimization examples discussed in our paper because the appropriate choice of $\ell_{\max}$ depends on the specific situations addressed. To improve the accuracy of the numerical results, we followed [9] and solved for the scaled equations as

$$\hat{\mathbf{T}}\hat{\mathbf{b}} = \hat{\mathbf{a}}^0, \tag{16}$$

$$\hat{\mathbf{b}} = b_{n\ell}/J_\ell(k_o r_n), \tag{17}$$

$$\hat{\mathbf{a}}^0 = a_{n\ell}/J_\ell(k_o r_n), \tag{18}$$

$$\hat{\mathbf{T}} = \delta_{nn'}\delta_{\ell\ell'} - (1-\delta_{nn'})\, e^{j(\ell'-\ell)\phi_{nn'}} \times H_{\ell-\ell'}(k_o R_{nn'})\, s_{n\ell}\frac{J_{\ell'}(k_o r_{n'})}{J_\ell(k_o r_n)}. \tag{19}$$

Detailed expressions for the incident wave coefficients $\mathbf{a}^0$ of plane waves, collimated source beams (similar to Gaussian beams but strictly a solution of the 2D Helmholtz equation), and the excitation dipoles can be found in [9,28].

B. Derivation of the Scattered Far-Field Amplitude

Once the scattered field of the array is obtained by Eq. (3), we can express in closed-form relevant far-field quantities used in the analysis of wave-scattering systems. In particular, we focus here on the scattering amplitude $F_z^{\text{sca}}(\theta)$, which is defined through the asymptotic far-field expression

$$\varphi_z^{\text{sca}}(r,\theta) = F_z^{\text{sca}}(\theta)\frac{e^{jk_o r}}{\sqrt{r}}, \tag{20}$$

where $r = |\mathbf{r}|$. The scattering amplitude can be derived from the scattered fields by evaluating Eq. (3) in the limit of $r \to \infty$. Specifically, considering the asymptotic form of the Hankel function $H_\ell(z) \sim \sqrt{\frac{2}{\pi z}}e^{j(z-\ell\pi/2-\pi/4)}$, we obtain

$$\varphi_z^{\text{sca}}(\mathbf{r}) \approx p_z \sum_{n=1}^{N}\sum_{\ell=-\ell_{\max}}^{\ell_{\max}} \sqrt{\frac{2}{\pi k_o \rho_n}}\, e^{j(k_o\rho_n - \ell\pi/2-\pi/4+\ell\theta_n)}. \tag{21}$$

Using the cosine law on the triangle shown in Fig. 2(a), we found that $\rho_n = \sqrt{r^2 + R_n^2 - r R_n\cos(\theta-\phi_n)}$. In the far-field limit $r \to \infty$, we further obtained

$$\rho_n \approx r - R_n\cos(\theta-\phi_n), \tag{22}$$

where (R_n, ϕ_n) are the positions of the nth cylinder in polar coordinates. Although the $\cos(\theta-\phi_n)$ term is small relative to r in the far field, it has a significant impact on the phasor term of Eq. (21); thus, it must be kept in the exponent. On the other hand, we can directly substitute ρ_n with r in the prefactor of Eq. (21). Therefore, we obtain

$$\varphi_z^{\text{sca}}(\mathbf{r}) \approx p_z\frac{e^{jk_o r}}{\sqrt{r}}\sqrt{\frac{2}{\pi k_o}}\sum_{n=1}^{N}\sum_{\ell=-\ell_{\max}}^{\ell_{\max}} \times \left[b_{n\ell}e^{-j[k_o R_n\cos(\theta-\phi_n)+\ell(\frac{\pi}{2}-\theta)+\frac{\pi}{4}]}\right]. \tag{23}$$

Finally, comparing Eqs. (20) and (23) yields the expression for the scattering amplitude, which is

$$F_z^{\text{sca}}(\theta) = p_z\sqrt{\frac{2}{\pi k_o}}\sum_{n=1}^{N}\sum_{\ell=-\ell_{\max}}^{\ell_{\max}}\left[b_{n\ell}e^{-j[k_o R_n\cos(\theta-\phi_n)+\ell(\frac{\pi}{2}-\theta)+\frac{\pi}{4}]}\right]. \tag{24}$$

Based on Eq. (24), we can further derive a closed-form analytical expression for the scattered far-field angular intensity, which is a key quantity of interest in directional radiation problems. The far-field angular intensity is found by substituting Eqs. (20) and (24) into the time-averaged Poynting vector expression

$$\langle \mathbf{S}^{\text{sca}}\rangle = \frac{1}{2}\text{Re}\left[\mathbf{E}^{\text{sca}}\times\mathbf{H}^{\text{sca}}\right]. \tag{25}$$

To remove the radial dependence of the far-field intensity, we multiplied Eq. (25) by the radial distance r. The far-field angular intensity is thus given by the limit of the product when $r \to \infty$, resulting in

$$I^{\text{sca}}(\theta) = \lim_{r\to\infty} r\langle \mathbf{S}^{\text{sca}}\rangle = \frac{1}{2Z_o p_z^2}|F_z^{\text{sca}}(\theta)|^2. \tag{26}$$

Based on the knowledge of the far-field angular intensity, quantitative information can be obtained on the directional scattering properties of the arrays through their differential scattering cross-section. This quantity is obtained by normalizing the far-field angular intensity by the incident intensity I_o. In 2D-GMT calculation $I_o = 1/(2Z_o)$ and we obtain

$$\frac{\partial\sigma^{\text{sca}}}{\partial\theta} = \frac{I^{\text{sca}}(\theta)}{I_o} = \frac{|F_z^{\text{sca}}|^2}{p_z^2}, \tag{27}$$

which is an expression for the differential scattering cross section that describes how efficiently the incident radiation is scattered along a given angular direction. It is of great importance in evaluating the performances of devices used for radiation engineering [29].

The scattering cross-section is calculated by the integration of Eq. (27) over the far-field scattering angle

$$\sigma^{\text{sca}} = \int_{-\pi}^{\pi}\frac{\partial\sigma^{\text{sca}}}{\partial\theta}\text{d}\theta = \frac{1}{I_o}\int_{-\pi}^{\pi} I^{\text{sca}}(\theta)\text{d}\theta. \tag{28}$$

Substituting Eq. (24) into Eq. (28), we obtain the analytical expression for the scattering cross-section as

$$\sigma^{\text{sca}} = \frac{2}{\pi k_o}\sum_{nn'\ell\ell'} b_{n\ell}b^*_{n'\ell'}J_{\ell-\ell'}(k_o R_{nn'})e^{j(\ell-\ell')\phi_{nn'}}, \tag{29}$$

where * denotes the complex conjugate of $b_{n'\ell'}$.

C. Derivation of the LDOS

The LDOS quantifies the number of electromagnetic modes into which photons of a given wavelength can be emitted at a specified position in space. The LDOS is particularly useful because it is related to experimentally observable quantities such as transmission gaps and the spontaneous decay rate of

embedded light sources inside nonhomogeneous photonic environments [23,30,31]. By comparing the LDOS in a photonic device to one in free space, we can characterize the degree of the enhancement or suppression of the light emission.

The LDOS is related to the imaginary part of the electric field Green tensor [32]

$$\rho(\mathbf{r};\lambda) = -\frac{4n_o^2}{c\lambda}\mathrm{Im}\{\mathrm{Tr}[\mathbf{G}^e(\mathbf{r},\mathbf{r};\lambda)]\}, \tag{30}$$

where $n_o = \sqrt{\epsilon_o \mu_o}$ is the refractive index of host medium, Im{·} denotes the imaginary part of a complex quantity, and Tr denotes the trace operation. The electric field Green tensor $\mathbf{G}^e(\mathbf{r},\mathbf{r}_s;\lambda)$ is the electric field response at spatial location $\mathbf{r} = (x, y)$ resulting from a source at position $\mathbf{r}_s = (x_s, y_s)$. In general, it is a second-rank tensor where the elements in column u represent the components of the total electric field vector $(G_{xu}, G_{yu}, G_{zu})^{\mathrm{T}}$ generated by the dipole source with the orientation parallel to the $u = x, y, z$ axes [28].

In the 2D-GMT formalism, the trace of the Green tensor equals the total electric field component located at the source position (x_s, y_s), along the given dipole orientation. Therefore, depending on the polarization of the dipole source, the LDOS can be written as [28]

$$\rho_{\mathrm{TE}} = -\frac{4n_o^2}{c\lambda}\mathrm{Im}\{G_{xx} + G_{yy}\}, \tag{31}$$

$$\rho_{\mathrm{TM}} = -\frac{4n_o^2}{c\lambda}\mathrm{Im}\{G_{zz}\}. \tag{32}$$

We emphasize here that the total electric field is equal to the sum of the scattered field and the incident field generated by the dipole source, which is

$$G_{uu} = E_u^{\mathrm{inc}} + E_u^{\mathrm{sca}}, \quad u = x, y, z. \tag{33}$$

We have derived the z component of the exterior scattered electric field in Eq. (3). The corresponding x and y components of the exterior scattered field can be readily obtained from the dynamic Maxwell's equation

$$-j\omega\epsilon\mathbf{E}^{\mathrm{sca}} = \nabla \times \mathbf{H}^{\mathrm{sca}} = \frac{\partial H_z^{\mathrm{sca}}}{\partial y}\hat{\mathbf{x}} - \frac{\partial H_z^{\mathrm{sca}}}{\partial x}\hat{\mathbf{y}}. \tag{34}$$

On the other hand, the components of the field excited by a 2D dipole (i.e., a line source) at any position have been obtained in [28] as

$$E_x^{\mathrm{inc}} = -\frac{j}{8}\left[H_0(k_o\rho) + H_2(k_o\rho)\cos(2\theta)\right], \tag{35}$$

$$E_y^{\mathrm{inc}} = -\frac{j}{8}\left[H_0(k_o\rho) - H_2(k_o\rho)\cos(2\theta)\right], \tag{36}$$

$$E_z^{\mathrm{inc}} = -\frac{j}{4}H_0(k_o\rho), \tag{37}$$

where (ρ, θ) are polar coordinates centered at source location (x_s, y_s). Applying Graf's theorem to Eqs. (35)–(37), we can obtain the source coefficients of the dipole, which are

$$a_{n\ell,x}^{0E} = -\frac{1}{8j}\left[H_{\ell+1}(k_oR_{ns})e^{-j(\ell+1)\theta_{ns}} + H_{\ell-1}(k_oR_{ns})e^{-j(\ell-1)\theta_{ns}}\right], \tag{38}$$

$$a_{n\ell,y}^{0E} = -\frac{1}{8j}\left[H_{\ell+1}(k_oR_{ns})e^{-j(\ell+1)\theta_{ns}} - H_{\ell-1}(k_oR_{ns})e^{-j(\ell-1)\theta_{ns}}\right], \tag{39}$$

$$a_{n\ell,z}^{0E} = \frac{1}{4j}H_0(k_oR_{ns})e^{-j\ell\theta_{ns}}, \tag{40}$$

where $R_{ns} = \sqrt{(x_s - x_n)^2 + (y_s - y_n)^2}$ and $\theta_{ns} = \tan^{-1}\left(\frac{y_s - y_n}{x_s - x_n}\right)$.

Substituting Eqs. (34)–(40) into Eq. (33), we obtain the expressions for the total field at the excitation dipole position with different orientations, which are

$$G_{xx} = -\frac{j}{8} + \sum_{n\ell} j b_{n\ell} e^{j\ell\theta_{ns}}\left[H_\ell'(k_oR_{ns})\sin(\theta_{ns}) + \frac{j\ell}{k_oR_{ns}}H_\ell(k_oR_{ns})\cos(\theta_{ns})\right], \tag{41}$$

$$G_{yy} = -\frac{j}{8} - \sum_{n\ell} j b_{n\ell} e^{j\ell\theta_{ns}}\left[H_\ell'(k_oR_{ns})\cos(\theta_{ns}) - \frac{j\ell}{k_oR_{ns}}H_\ell(k_oR_{ns})\sin(\theta_{ns})\right], \tag{42}$$

$$G_{zz} = -\frac{j}{4} + \sum_{n\ell} b_{n\ell} H_\ell(k_oR_{ns})e^{j\ell\theta_{ns}}, \tag{43}$$

where $\sum_{n\ell} \equiv \sum_{n=1}^{N}\sum_{\ell=-\ell_{\max}}^{\ell_{\max}}$. Note that the constant terms in the equations above originate from selecting the observation point exactly at the source location; i.e., by setting $\rho = 0$ in Eqs. (35)–(37).

Based on the expressions above for the LDOS, we can obtain the Purcell enhancement factor $\mathrm{F}(\mathbf{r};\lambda)$, which characterizes the modification of the LDOS in the presence of a structured photonic environment with respect to a homogeneous medium, here assumed to be free space. The Purcell factor is generally defined as

$$\mathrm{F}(\mathbf{r};\lambda) = \frac{\rho(\mathbf{r};\lambda)}{\rho_0(\mathbf{r};\lambda)} = -4\,\mathrm{Im}\left\{\mathrm{Tr}[\mathbf{G}^e(\mathbf{r},\mathbf{r};\lambda)]\right\} = \frac{\Gamma(\mathbf{r};\lambda)}{\Gamma_0(\mathbf{r};\lambda)}, \tag{44}$$

where ρ_0 is the LDOS of the homogeneous host medium, Γ_0 is the decay rate of a dipole in the homogeneous medium, and Γ is its decay rate in the structured environment. Notice that $\mathrm{F}(\mathbf{r};\lambda)$ becomes unity when the source is embedded in the homogeneous medium. On the other hand, $\mathrm{F}(\mathbf{r};\lambda) > 1$ indicates that the photonic structure enhances the radiative properties of the dipole, while spontaneous emission is suppressed when $\mathrm{F}(\mathbf{r};\lambda) < 1$.

2. ADJOINT OPTIMIZATION COUPLED WITH 2D-GMT

In this section, we provide an overview of the general adjoint optimization method and discuss the details of its coupling

to the 2D-GMT when applied to finite-sized arrays of dielectric nanocylinders. We will then show how to inverse design photonic patches engineered to shape the far-field radiation, focus incident radiation in the Fresnel zone, and enhance the LDOS and the quality factor Q of resonant modes at different wavelengths.

A. Adjoint Optimization Method

Suppose we define an objective function $\mathrm{g}(\hat{\mathbf{b}}, \mathbf{p})$ that depends on both the scattered field coefficients $\hat{\mathbf{b}}$ and a vector of design parameters $\mathbf{p}$. These may include the positions and radii of each cylinder, their composition, among other things. The key quantity to compute is the gradient of g with respect to $\mathbf{p}$, which is written as

$$\nabla_{\mathbf{p}}\mathrm{g}(\hat{\mathbf{b}}, \mathbf{p}) = \mathrm{g}_{\mathbf{p}} + \mathrm{g}_{\hat{\mathbf{b}}}\hat{\mathbf{b}}_{\mathbf{p}}, \tag{45}$$

where the subscript symbols indicate partial derivative operations with respect to those quantities; i.e., $\mathrm{g}_{\mathbf{p}} = \partial \mathrm{g}/\partial \mathbf{p}$, $\mathrm{g}_{\hat{\mathbf{b}}} = \partial \mathrm{g}/\partial \hat{\mathbf{b}}$, and $\hat{\mathbf{b}}_{\mathbf{p}} = \partial \hat{\mathbf{b}}/\partial \mathbf{p}$. Notice that the term $\hat{\mathbf{b}}_{\mathbf{p}}$ is generally computationally expensive to evaluate when using any full numerical method, such as FDTD or FEM, because it requires at least two simulations for each design parameter stored in the vector $\mathbf{p}$ [1]. However, as we have shown in Section 1, the 2D-GMT solves the scattering problem analytically with the T matrix equation Eq. (16) and provides efficient evaluation of closed-form solutions for the forward simulations. To leverage this advantage, we first take the derivative with respect to $\mathbf{p}$ on both sides of Eq. (16), which yields

$$\hat{\mathbf{T}}_{\mathbf{p}}\hat{\mathbf{b}} + \hat{\mathbf{T}}\hat{\mathbf{b}}_{\mathbf{p}} = \hat{\mathbf{a}}^0_{\mathbf{p}}, \tag{46}$$

where $\hat{\mathbf{T}}_{\mathbf{p}} = \partial\hat{\mathbf{T}}/\partial\mathbf{p}$ and $\hat{\mathbf{a}}^0_{\mathbf{p}} = \partial\hat{\mathbf{a}}^0/\partial\mathbf{p}$. After rearranging the terms, we obtain

$$\hat{\mathbf{b}}_{\mathbf{p}} = \hat{\mathbf{T}}^{-1}\left[\hat{\mathbf{a}}^0_{\mathbf{p}} - \hat{\mathbf{T}}_{\mathbf{p}}\hat{\mathbf{b}}\right]. \tag{47}$$

Crucially, substituting Eq. (47) in Eq. (45), the expression for the gradient term can be written as

$$\nabla_{\mathbf{p}}\mathrm{g}(\hat{\mathbf{b}}, \mathbf{p}) = \mathrm{g}_{\mathbf{p}} + \mathrm{g}_{\hat{\mathbf{b}}}\left(\hat{\mathbf{T}}^{-1}\left[\hat{\mathbf{a}}^0_{\mathbf{p}} - \hat{\mathbf{T}}_{\mathbf{p}}\hat{\mathbf{b}}\right]\right). \tag{48}$$

Equation (48), which enables the efficient calculation of the parameterized gradient within the T matrix formalism, is the main result of this section. This result is often expressed in the literature as [33]

$$\nabla_{\mathbf{p}}\mathrm{g} = \mathrm{g}_{\mathbf{p}} + \mathrm{Re}\left\{\boldsymbol{\lambda}^{\mathrm{T}}\left[\hat{\mathbf{a}}^0_{\mathbf{p}} - \hat{\mathbf{T}}_{\mathbf{p}}\hat{\mathbf{b}}\right]\right\}, \tag{49}$$

$$\hat{\mathbf{T}}^{\mathrm{T}}\boldsymbol{\lambda} = \mathrm{g}^{\mathrm{T}}_{\hat{\mathbf{b}}}, \tag{50}$$

where $\boldsymbol{\lambda} = (\hat{\mathbf{T}}^{\mathrm{T}})^{-1}\mathrm{g}^{\mathrm{T}}_{\hat{\mathbf{b}}}$, the superscript T indicates the transpose operation, and Eq. (50) is referred to as the adjoint equation [1]. The $\mathrm{Re}\{\cdot\}$ operator in Eq. (49) comes from the result of the Wirtinger derivative in complex space, which is elaborated in [33]. Equations (49) and (50) enable the efficient computation of the gradient based on only a single forward simulation to obtain the coefficient $\hat{\mathbf{b}}$. The derivative quantities $\hat{\mathbf{T}}_{\mathbf{p}}$, $\hat{\mathbf{a}}^0_{\mathbf{p}}$ are evaluated analytically using the previously established results of the 2D-GMT theory and their explicit expressions are provided in Appendixes A–C. In the next subsection, we will discuss the explicit calculations of the derivatives $\mathrm{g}_{\hat{\mathbf{b}}}$ and $\mathrm{g}_{\mathbf{p}}$ for different choices of the objective function associated to different properties of interest of the cylinder arrays and we will also discuss specific optimization cases.

B. Inverse Design of Photonic Patches for Radiation Shaping

In this subsection, we apply the adjoint method to the specific design of "photonic patches," which are compact arrays of nanocylinders (∼100 elements) that occupy a small footprint area and exhibit an optimal functionality. In particular, we begin by presenting our results on the design of photonic patches that can efficiently steer incoming radiation of different wavelengths into desired far-field angles.

To optimize the directional radiation properties of photonic patches, we considered the objective function defined by the scattering intensity at the desired angle θ_o and wavelength λ_o, which is

$$\mathrm{g}(\mathbf{r}, \hat{\mathbf{b}}) = I^{\mathrm{sca}}(\theta_o, \lambda_o) = \frac{1}{2Z_o p_z^2}|F_z^{\mathrm{sca}}(\theta_o, \lambda_o)|^2, \tag{51}$$

where $F_z^{\mathrm{sca}}(\theta)$ is the scattering amplitude provided in Eq. (24). To apply the adjoint optimization method, we first had to obtain the expressions for $\mathrm{g}_{\mathbf{p}}$ and $\mathrm{g}_{\hat{\mathbf{b}}}$. For the ith $(I = 1, 2, \ldots, P)$ component of the vector $\mathrm{g}_{\mathbf{p}}$, we get

$$\frac{\partial I(\theta_o, \lambda_o)}{\partial p_i} = \frac{1}{Z_o p_z^2}\mathrm{Re}\left\{\left(F_z^{\mathrm{sca}}\right)^* \frac{\partial F_z^{\mathrm{sca}}}{\partial p_i}\right\}, \tag{52}$$

where $\mathrm{Re}\{\cdot\}$ denotes the real part of the complex quantity and * denotes its complex conjugate. Combining this expression with Eq. (24), we obtained

$$\frac{\partial I(\theta)^{\mathrm{sca}}}{\partial p_i} = \frac{-jk_o}{Z_o}\left(\sum_{n\ell}\hat{b}_{n\ell}\gamma_{n\ell}\right)^* \times \left(\sum_{n\ell}\hat{b}_{n\ell}\gamma_{n\ell}\left[k_o\frac{J'_\ell(k_o r_n)}{J_\ell(k_o r_n)} \times \frac{\partial r_n}{\partial p_i} + R_n\sin(\theta-\phi_n)\frac{\partial \phi_n}{\partial p_i} + \cos(\theta-\phi_n)\frac{\partial R_n}{\partial p_i}\right]\right), \tag{53}$$

where $\gamma_{n\ell} = \sqrt{\frac{2}{\pi k_o}}J_\ell(k_o r_n)e^{-j[k_o R_n\cos(\theta-\phi_n)+\ell(\pi/2-\theta)+\pi/4]}$. The expressions for the derivatives of the geometrical parameters of the array with respect to the considered design parameters (i.e., the positions and radii of each cylinder), can be found in Table 1.

In Table 1, the design parameters (x_j, y_j) and r_j correspond to the center coordinates and radius of each jth cylinder in the

Table 1. Derivatives of the Array Geometry with Respect to the Design Parameters

$\partial r_n/\partial x_j = 0$	$\partial r_n/\partial y_j = 0$	$\partial r_n/\partial r_j = \delta_{ni}$
$\partial R_n/\partial x_j = \cos(\phi_n)\delta_{nj}$	$\partial R_n/\partial y_j = \sin(\phi_n)\delta_{nj}$	$\partial R_n/\partial r_j = 0$
$\frac{\partial \phi_n}{\partial x_j} = -\frac{\sin(\phi_n)}{R_n}\delta_{nj}$	$\frac{\partial \phi_n}{\partial y_j} = \frac{\cos(\phi_n)}{R_n}\delta_{nj}$	$\frac{\partial \phi_n}{\partial r_j} = 0$

array. The expression for $g_{\hat{\mathbf{b}}}$ can be obtained from Eq. (24) as

$$\frac{\partial I^{\mathrm{sca}}(\theta)}{\partial \hat{b}_{n\ell}} = \frac{1}{Z_o}\gamma_{n\ell}\left(\sum_{m=1}^{N}\sum_{p=-\ell_{\max}}^{\ell_{\max}} \hat{b}_{mp}\gamma_{mp}\right)^{*}. \tag{54}$$

Now we have computed all the analytical derivatives needed to perform the adjoint optimization of directional photonic patches within the framework of the 2D-GMT. These are compact photonic systems with optimized far-field scattered intensity at angle θ_o and wavelength λ_o. As a concrete demonstration of the developed method, we optimized for both the positions and the radii of the individual nanocylinders in a photonic patch to achieve simultaneous steering of radiation at wavelengths λ_1 and λ_2 and angles θ_1 and θ_2, respectively. Therefore, we introduced the objective function

$$\mathrm{g} = \frac{1}{I^{\mathrm{sca}}(\theta_1, \lambda_1)} + \frac{1}{I^{\mathrm{sca}}(\theta_2, \lambda_2)}. \tag{55}$$

We used the gradient descent method to update the design parameters in each iteration. Specifically, at the kth iteration, we have

$$\mathbf{p}^{\mathrm{k}} \leftarrow \mathbf{p}^{\mathrm{k}-1} - \alpha\frac{\partial \mathrm{g}^{\mathrm{k}-1}}{\partial \mathbf{p}^{\mathrm{k}-1}}, \tag{56}$$

where α is the learning rate. The objective function value will decrease in each iteration and the far-field intensities $I^{\mathrm{sca}}(\theta_1, \lambda_1)$ and $I^{\mathrm{sca}}(\theta_2, \lambda_2)$ will increase by optimizing the design parameters. In our optimization, we chose $\lambda_1 = 1.0$ μm, $\lambda_2 = 1.1$ μm, $\theta_1 = 50°$, and $\theta_2 = 70°$ for the parameters of the objective function in Eq. (55). The excitation was set to be a TM-polarized complex source beam (CSB). These beams are rigorous solutions of the scalar Helmholtz equation beyond the usual paraxial approximation, as discussed in [9]. In our calculations, we chose the beam width to be $\sigma = 4$ μm so that the incident beam did not overfill the photonic patch. We used a learning rate equal to 0.2 to update the cylinder radii and 0.02 to update their center positions. During our 2D-GMT calculations, the maximum angular order was set to $\ell_{\max} = 3$, which is large enough to produce accurate results.

We started from an initial array of 99 cylinders arranged in the Vogel spiral structure, which is defined in polar coordinates as

$$\begin{cases} r_n = a_0\sqrt{n} \\ \theta_n = n\alpha \end{cases}, \tag{57}$$

where $n = 0, 1, 2, \ldots$ is an integer, a_0 is a positive constant called the scaling factor, and α is an irrational number, known as the divergence angle [34]. Specifically for GA, Vogel spirals $\alpha = 360°/\phi^2$, where $\phi = (1+\sqrt{5})/2 \approx 1.618$ is known as the golden number. The divergence angle determines the constant aperture between successive point particles in the array. Since it is an irrational number, Vogel spiral arrays lack both translational and rotational symmetry. Vogel spiral structures have been largely investigated in plasmonics and nanophotonics due to their unique light scattering and localization properties that enable compact photonic devices with broadband enhanced light–matter interactions [18,19,24,35–40].

In our simulations we considered an initial GA Vogel spiral array with an averaged center-to-center particle separation of ~1 μm. We also set the initial cylinder radii as $r = 300$ nm, and the permittivity for the nanocylinder material as $\epsilon = 2.25$. We also considered the practical limitations of our current fabrication technology and set the minimum radius for all cylinders to be no less than 50 nm during the optimization. Furthermore, to avoid the cylinders overlapping during the optimization, we evaluated the first-neighbor distances of the array based on the updated positions and radii during each iteration and rejected any configuration in which the cylinders overlapped. A small value of the permittivity allows us to take advantage of long-range coupling effects across the entire array of nanocylinders, making its geometrical optimization more effective in this limit, and Fig. 14 shows the results obtained with different permittivity values. We displayed the initial array geometry in Fig. 3(a). We optimized more than 200 iterations, and the value of the objective function during the optimization process is shown in Fig. 3(c). Convergence is obtained around $\mathrm{g} \sim 1$. Furthermore, the optimized array geometry is shown in Fig. 3(b). We observed that in the optimal array the cylinder radii are not all equal and the positions of each cylinder are also shifted with respect to the initial GA geometry. The spatial distributions of the total electric field for the initial array geometry excited by a TM-polarized CSB at wavelengths λ_1 and λ_2, respectively, are shown in Figs. 3(d) and 3(g). Figures 3(e) and 3(h) display the total field of the optimized array geometry. Figure 3(f) has a polar plot of the obtained far-field intensities when the initial structure is illuminated at wavelengths λ_1 and λ_2, which indicates almost isotropic intensity distributions. For comparison, the obtained far-field intensities are shown in Fig. 3(i) at the illuminating wavelengths λ_1 and λ_2 on the optimized structure. In this case, the far-field pattern clearly demonstrates high directionality and that the incident wavelengths λ_1 and λ_2 are correctly steered in the desired angular directions of 50° and 70°, respectively. The differential scattering efficiencies of λ_1, λ_2, which are defined by the ratio of total radiated light power along θ_1, θ_2 and their corresponding input power, which is 1 W in our calculation [9,29], are estimated to be, respectively, 53% and 60%. Note that with a CSB as the incident source, the differential scattering efficiency along a given angle is equal to the integrated far-field intensity in a small interval around the directional angle [9]. The expression for the differential scattering cross-section is given in Eq. (27). The efficiency values we obtained in the optimized photonic patches are comparable to what has been achieved in beam-steering applications using metasurface technologies [29,41–45].

We compared the optimization results of the GA Vogel spiral geometry with an 11×9 periodic nanocylinder array characterized by the same averaged interparticle distance 1 μm. The objective function parameters, learning rates, and maximum multipole order ℓ are chosen to be the same as in the GA Vogel spiral case. Figures 4(a) and 4(b) show the initial and optimized array geometries. Figure 4(c) shows the convergence achieved around $\mathrm{g} \sim 1$, similar to the case with GA Vogel spiral. Figures 4(d) and 4(g) show the spatial distribution of the total electric field for the initial structures at λ_1 and λ_2, while Figs. 4(e) and 4(h) show the results for the optimized structures, respectively. Figures 4(f) and 4(i) shows the polar plot representations of the computed far-field intensity patterns at both the wavelengths for the initial and the optimized geometries,

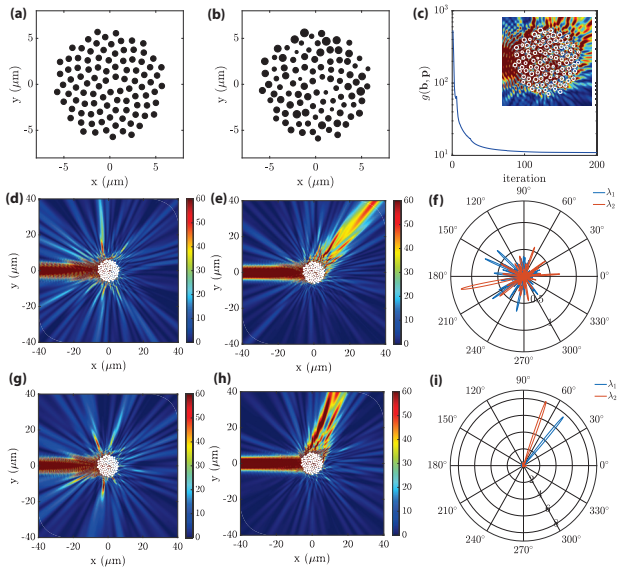

Fig. 3. Example of a photonic patch optimized starting from a GA Vogel spiral for steering incident radiation of two selected wavelengths into two desired directions. (a) Initial geometry of the GA Vogel spiral structure. (b) Optimized geometry of the photonic patch. (c) Objective function value as a function of the number of iterations. The inset shows the total electric field inside the photonic patch. (d) and (g) Total electric field intensity distribution of the initial geometry under TM excitation using a complex source beam (CSB) at the wavelengths λ_1 and λ_2, respectively. (e) and (h) Field distribution of the optimized geometry at the same wavelengths. Total far-field intensity radiation diagrams at λ_1 and λ_2 for (f) the initial geometry and (i) the optimized geometry.

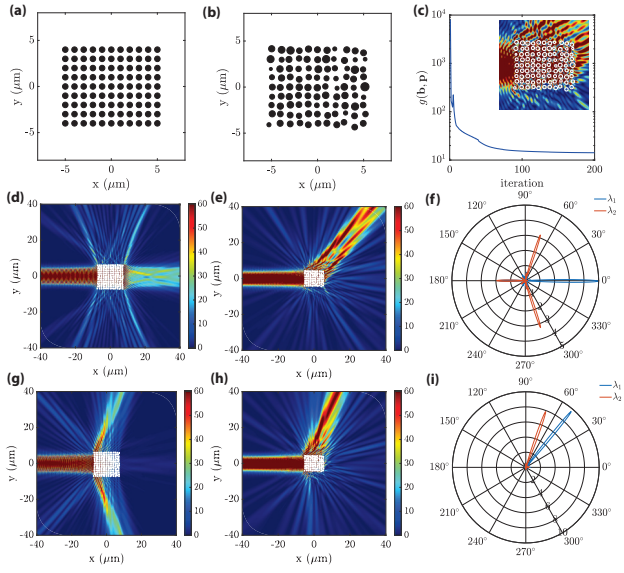

Fig. 4. Example of a photonic patch optimized starting from a periodic geometry to steer the incident radiation of two selected wavelengths into two desired directions. (a) Initial geometry of the periodic structure. (b) Optimized photonic patch geometry. (c) Objective function value as a function of the number of iterations. The inset shows the total electric field inside the photonic patch. (d) and (g) Total electric field intensity distribution of the initial geometry under TM excitation using a complex source beam (CSB) at the wavelengths λ_1 and λ_2, respectively. (e) and (h) Field distribution of the optimized geometry at the same wavelengths. Total far-field intensity radiation diagrams at λ_1 and λ_2 for (f) the initial geometry and (i) the optimized geometry.

respectively. The obtained differential scattering efficiencies at λ_1, λ_2 are 51% and 60%, respectively.

To further demonstrate the potential of our adjoint optimization method in the context of multiwavelength radiation shaping, we optimized photonic patches that simultaneously steer incident waves at four different wavelengths into four desired far-field angles. The objective function that we used in this case is

$$\mathrm{g} = \sum_{i=1}^{4} \frac{1}{I^{\mathrm{sca}}(\theta_i, \lambda_i)}. \tag{58}$$

In this example, we selected $\lambda_1 = 1.0\ \mu\mathrm{m}$, $\lambda_2 = 1.1\ \mu\mathrm{m}$, $\lambda_3 = 1.2\ \mu\mathrm{m}$, $\lambda_4 = 1.3\ \mu\mathrm{m}$, $\theta_1 = 50°$, $\theta_2 = 140°$, $\theta_3 = 230°$, and $\theta_4 = 320°$. The learning rate for updating radii and positions as well as $\ell_{\max}$ were kept the same as in the case of the previous optimizations. Similarly, we compared the results of an optimized GA Vogel spiral photonic patch to the ones of an optimized periodic array. The optimal GA Vogel spiral geometry is shown in Fig. 5(a). Moreover, Figs. 5(b)–5(e) show the total intensity distributions on the arrays at the four targeted wavelengths. The polar plot radiation diagram displayed in Fig. 5(f) demonstrates the ability of the optimized patch to steer incident radiation along the desired direction angles at each wavelength. The steering efficiencies at the four wavelengths were found to be 43%, 53%, 50%, and 53%. The corresponding results obtained by optimizing the periodic array are illustrated in Fig. 6. In this case, the steering efficiencies at the four wavelengths were found to be 52%, 56%, 54%, and 60%. These results indicate that optimized photonic patches for multiwavelength beam steering produce similar results regardless of the initial array geometry. Therefore, we have shown that our proposed approach can be used for the robust inverse design of photonics patches with small footprints that steer multiple wavelengths to desired directions.

C. Inverse Design of Photonic Patches for Radiation Focusing

In this section, we apply our inverse design methodology to optimize the focusing of incident radiation in the Fresnel zone using photonics patches. Specifically, we want to maximize the field intensity at a specific point (x_f, y_f) under TM plane wave excitation for a generic wavelength λ_o. Our objective function is therefore

$$\mathrm{g} = \frac{1}{I_z^{\mathrm{sca}}(x_f, y_f; \lambda_o)} = \frac{1}{|\varphi_z^{\mathrm{sca}}(x_f, y_f; \lambda_o)|^2}, \tag{59}$$

where $\varphi_z^{\mathrm{sca}} \equiv \varphi_z^{E,\mathrm{sca}}$ was defined in Eq. (3). To enable the optimization of the focusing properties we computed the partial derivative of g with respect to the design parameters p_i by

$$\frac{\partial \mathrm{g}}{\partial p_i} = -\frac{2}{(I_z^{\mathrm{sca}}(x_f, y_f; \lambda_o))^2} \mathrm{Re}\left\{ \frac{\partial \varphi_z^{\mathrm{sca}}}{\partial p_i} (\varphi_z^{\mathrm{sca}})^* \right\}, \tag{60}$$

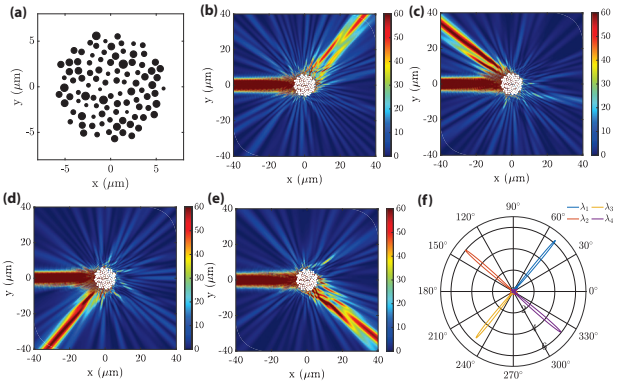

Fig. 5. Example of a photonic patch optimized starting from the GA Vogel spiral geometry that steers four wavelengths into four desired directions. (a) Optimized photonic patch geometry. Total electric field intensity distributions under TM excitation using a CSB at wavelengths (b) $\lambda_1 = 1.0$ μm, (c) $\lambda_2 = 1.1$ μm, (d) $\lambda_3 = 1.2$ μm, and (e) $\lambda_4 = 1.3$ μm, respectively. (f) Total far-field intensity radiation diagram at λ_1 through λ_4.

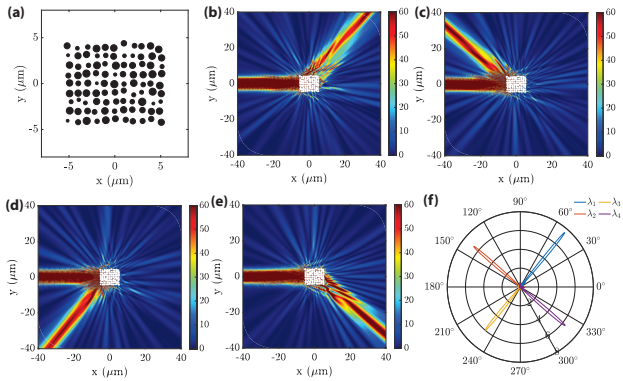

Fig. 6. Example of a photonic patch optimized starting from a square array geometry that steers four wavelengths into four directions. (a) Optimized photonic patch geometry. Total electric field intensity distributions under TM excitation using a CSB at wavelengths (b) $\lambda_1 = 1.0$ μm, (c) $\lambda_2 = 1.1$ μm, (d) $\lambda_3 = 1.2$ μm, and (e) $\lambda_4 = 1.3$ μm, respectively. (f) Total far-field intensity radiation diagram at λ_1 through λ_4.

where we have

$$\frac{\partial \varphi_z^{\text{sca}}}{\partial p_i} = \sum_{n\ell} \hat{b}_{n\ell} \tau_{n\ell} \left[k_o \frac{J_\ell'(k_o r_n)}{J_\ell(k_o r_n)} \frac{\partial r_n}{\partial p_i} + k_o \frac{H_\ell'(k_o \rho_n)}{H_\ell(k_o \rho_n)} \frac{\partial \rho_n}{\partial p_i} + j\ell \frac{\partial \theta_n}{\partial p_i} \right], \tag{61}$$

and we defined $\tau_{n\ell} = p_z J_\ell(k_o r_n) H_\ell(k_o \rho_n) e^{j\ell\theta_n}$. Furthermore, the derivative of $g_{\hat{\mathbf{b}}}$ can be computed as

$$\frac{\partial g}{\partial \hat{b}_{n\ell}} = 2\,\text{Re}\left\{ \frac{\partial \varphi_z^{\text{sca}}}{\partial \hat{b}_{n\ell}} (\varphi_z^{\text{sca}})^* \right\}, \tag{62}$$

where

$$\frac{\partial \varphi_z^{\text{sca}}}{\partial \hat{b}_{n\ell}} = \tau_{n\ell} (\varphi_z^{\text{sca}})^*. \tag{63}$$

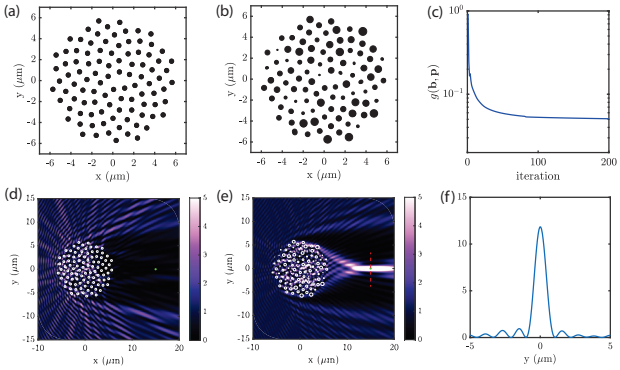

Fig. 7. Example of a focusing photonic patch optimized starting from the GA Vogel spiral geometry. (a) Initial photonic patch geometry. (b) Optimized focusing patch geometry. (c) Objective function value with respect to the number of iterations. Total electric field intensity distributions for (d) initial and (e) optimized arrays under a TM plane wave excitation at $\lambda = 1$ μm. The green dots in (d) and (e) indicate the targeted focal position (15 μm, 0). (f) Transverse profile of the focal spot along the red dashed line shown in (e).

In our focusing simulation we chose $\lambda = 1$ μm and $(x_f, y_f) = (15\ \mu\text{m}, 0)$. We started from an initial array with 99 cylinders arranged in a GA Vogel spiral, the same condition as discussed in Subsection 2.B. We set the initial cylinder radii $r = 200$ nm and fix the permittivity of the nanocylinders material to be $\epsilon = 2.25$. The maximum angular order is chosen as $\ell_{\max} = 4$ to improve the accuracy in the near-field zone. We display the initial cylinder array geometry in Fig. 7(a). We use the same learning rates to update radii and positions as in the Subsection 2.B. We optimize the radii and centers of the cylinders in the array using 200 iterations. The optimized array geometry of the patch is shown in Fig. 7(b), where we clearly observe that the positions and radii of cylinders have been modified from the ones in the initial structure. The objective function with respect to the number of iterations is shown in Fig. 7(c). Furthermore, we show the total field intensities for both the initial and the optimized arrays under plane wave excitation at wavelength λ in Fig. 7(d) and 7(e), respectively. The profile of the focal spot along the $x_f = 15$ μm line is shown in Fig. 7(f). The transverse FWHM of the focusing spot is 0.98 μm. The focusing efficiency, which is defined as the ratio between the power contained in the main lobe of the focal spot and that of the incident power deposited on the area of the device, is calculated to be 77%.

As a comparison, we also optimized a 99-cylinder array starting from a periodic square structure. Keeping all the parameters the same as in the case of the GA Vogel spiral simulation, we display the initial and optimized array geometries in Fig. 8(a) and 8(b). Fig. 8(c) shows the values of the objective function with respect to the number of iterations. Similar to the case of the GA Vogel spiral, Fig. 8(d) and 8(e) display the spatial distributions of the total field intensity for the initial and the optimized array geometries, respectively. In Fig. 8(f), we illustrate the transverse profile of the focal spot along the $x_f = 15$ μm dashed line. The transverse FWHM of the focusing spot is also 0.98 μm. We can clearly observe that the field intensity at the desired location (indicated by the red dot) is strongly enhanced. The intensity

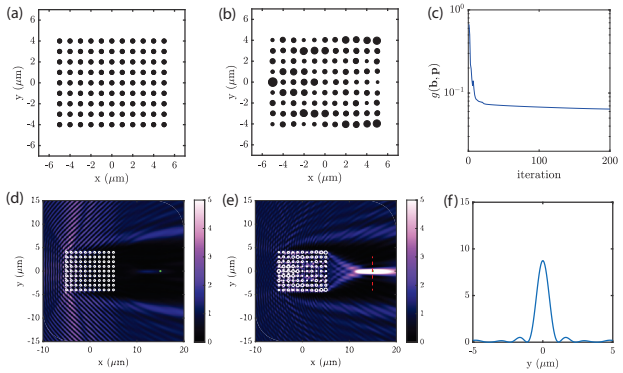

Fig. 8. Example of a focusing photonic patch optimized starting from a periodic square array. (a) Initial photonic patch geometry. (b) Optimized focusing patch geometry. (c) Objective function value with respect to the number of iterations. Total electric field intensity distributions for (d) initial and (e) optimized arrays under a TM plane wave excitation at $\lambda = 1$ μm. The green dot in (d) and (e) indicates the targeted focal position (15 μm, 0). (f) The transverse profile of the focal spot along the red dashed line shown in (e).

profile is similar to that of a focusing lens. However, we emphasize that here we are achieving such a focusing behavior using an array of cylinders with a total dimension of ∼10 μm and a focal length $x_f = 15$ μm, which are challenging to obtain using traditional diffractive elements. In addition, we found that the focusing efficiency of the optimized periodic patch is 60%. It is noteworthy to observe that if one considers a diffraction-limited lens with the same diameter and dimension of the optimized photonic patch as well as the same focal length as 15 μm, then the FWHM of at the focal spot according to Rayleigh criterion will be 1.58 μm [46]. This behavior reflects the structural complexity of the optimized aperiodic geometries of the patches which, analogously to what recently reported in random media [47,48], produce a focal spot with significantly smaller FWHM compared to the traditional Rayleigh diffraction limit.

We further optimized photonic patches that can focus incident light at different focal lengths. Figures 9 and 10 show the total field intensity patterns of six different devices with focal positions at $x_f = 10, 15, 20, 25, 30, 35$ μm, for the initial GA Vogel spiral geometry and periodic geometry, respectively. The incident wavelength for all devices is $\lambda = 1$ μm. The focusing efficiencies obtained for the GA Vogel spiral and periodic geometry, for different focal positions x_f are listed in Fig. 11(a). Our results indicate that when considering only one focusing wavelength, the focusing efficiencies of the optimized GA Vogel spiral patches and periodic patches are quite comparable. However, it is also very relevant to consider the case of broadband incident radiation, which we address below.

The goal is to investigate the inverse design of optimized photonic patches for broadband focusing applications. This can be achieved by considering the multi-objective function defined as

$$g = \sum_{i=1}^{5} \frac{1}{I_z^{\mathrm{sca}}(x_f, y_f; \lambda_i)} + \sum_{i \neq j} \left[I_z^{\mathrm{sca}}(x_f, y_f; \lambda_i) - I_z^{\mathrm{sca}}(x_f, y_f; \lambda_j) \right]^2. \quad (64)$$

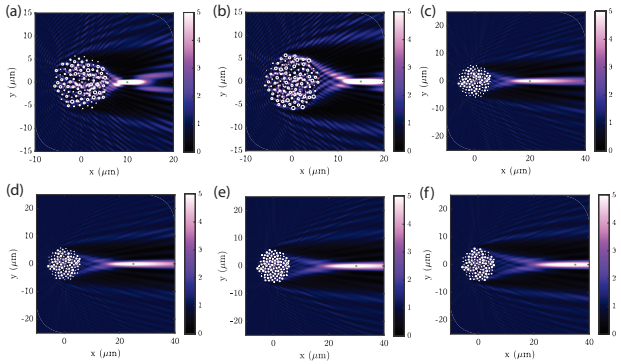

Fig. 9. Six different optimized photonic patches obtained starting from the GA spiral geometry. These patches focus incident light at the desired focal positions x_f given by (a) 10 μm, (b) 15 μm, (c) 20 μm, (d) 25 μm, (e) 30 μm, and (f) 35 μm. The y_f coordinates for all cases are 0. The considered wavelength for the incident plane wave is 1 μm.

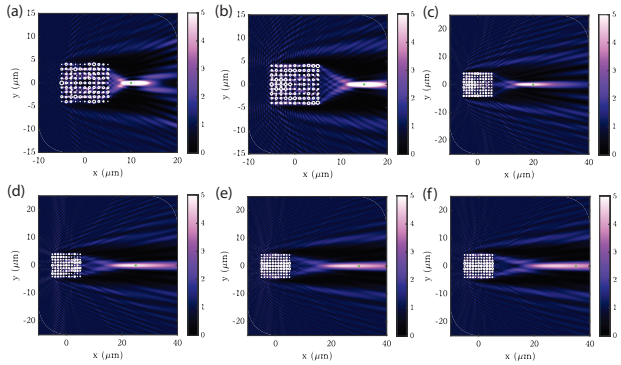

Fig. 10. Six different optimized photonic patches obtained starting from the square array geometry. These patches focus incident light at the desired focal positions x_f given by (a) 10 μm, (b) 15 μm, (c) 20 μm, (d) 25 μm, (e) 30 μm, and (f) 35 μm. The y_f coordinates for all cases are 0. The considered wavelength for the incident plane wave is 1 μm.

Note that the summation over all wavelengths ensures that the focal spot intensities at multiple incident wavelengths are mutually maximized. To prevent the situation where the focal intensity of only one wavelength is maximized, we introduced above a cross term that penalizes large focal intensity differences for any pair of distinct wavelengths. To illustrate the approach, we selected the five incident wavelengths $\lambda_1 = 1.0$ μm, $\lambda_2 = 1.1$ μm, $\lambda_3 = 1.2$ μm, $\lambda_4 = 1.3$ μm, $\lambda_5 = 1.4$ μm and the focal position was chosen to be $(x_f, y_f) = (10$ μm, 0). To consider a realistic implementation of integrated focusing components with an achromatic behavior, we used a TM-polarized CSB excitation with the same beam parameters introduced in Subsection 2.B. We optimized the patches using a learning rate of 0.2 to update the cylinder radii and that of 0.02 to update cylinder positions, and the total number of iterations used here was 1000. Figure 12 illustrates the total field intensity distributions of the device optimized starting from a GA Vogel spiral geometry, while Fig. 13 illustrates those of the optimized periodic devices. The focusing efficiencies obtained for the GA Vogel spiral and periodic geometries are compared at the different incident wavelengths λ in Fig. 11(b). Note that the

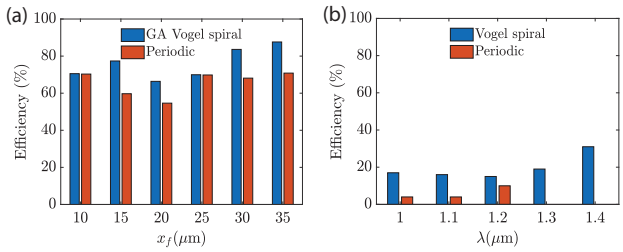

Fig. 11. (a) Single wavelength ($\lambda = 1$ μm) focusing efficiencies for optimized GA Vogel spirals (blue) and periodic array (red) photonic patches with different focal positions x_f. (b) Broadband focusing efficiencies of optimized GA Vogel spiral (blue) and periodic array (red) achromatic patches at different incident wavelengths λ. The focusing positions are all $(x_f, y_f) = (10\ \mu m, 0)$.

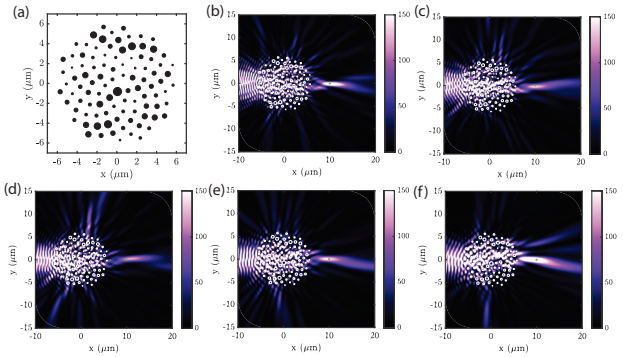

Fig. 12. (a) Optimized GA Vogel spiral geometry for achromatic focusing at $x_f = 10$ μm. Also shown are the field intensity distributions with incident wavelengths (b) $\lambda_1 = 1.0$ μm, (c) $\lambda_2 = 1.1$ μm, (d) $\lambda_3 = 1.2$ μm, (e) $\lambda_4 = 1.3$ μm, and (f) $\lambda_5 = 1.4$ μm.

optimized periodic patch does not appreciably focus incident light at wavelengths $\lambda_4 = 1.3$ μm and $\lambda_5 = 1.4$ μm; therefore, the focusing efficiencies could not be defined for those values. From our analysis we concluded that while the focusing performances at a single wavelength are comparable for the two considered geometries, the optimized GA aperiodic patches show significant efficiency advantages in broadband focusing compared to the optimized periodic arrays.

We finally characterized the focusing efficiency of photonic patches as a function of the permittivity ϵ of the dielectric cylinders. We directly compared arrays optimized starting from the GA Vogel spiral and the square array configurations, using the same structural parameters as in Figs. 7(a) and 8(b). The focal distance was set to $x_f = 15$ μm, $y_f = 0$ and the wavelength was $\lambda = 1$ μm. Figures 14(a) and 14(b) show how the focusing efficiencies decrease when ϵ is increased for both configurations. This behavior reflects the more localized nature of the resonances supported for larger ϵ, reducing long-range electromagnetic coupling and the effectiveness of the geometrical optimization in this limit [49–51].

D. Scaling Analysis of Photonic Patches

A key question in the design of photonic patches is related to what is the smallest size of the array that still achieves a desired functionality. To answer that question, we systematically

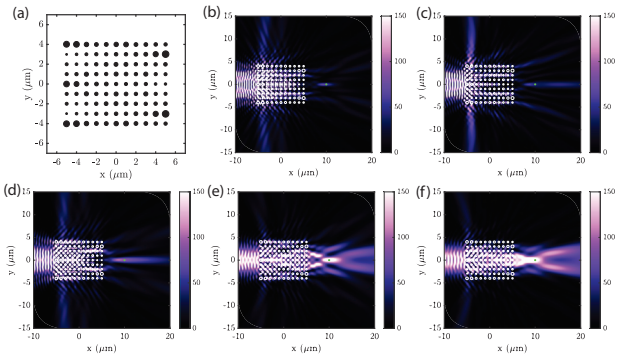

Fig. 13. (a) Optimized periodic array photonic patch for achromatic focusing at $x_f = 10$ μm. Also shown are the field intensity distributions with incident wavelengths (b) $\lambda_1 = 1.0$ μm, (c) $\lambda_2 = 1.1$ μm, (d) $\lambda_3 = 1.2$ μm, (e) $\lambda_4 = 1.3$ μm, and (f) $\lambda_5 = 1.4$ μm.

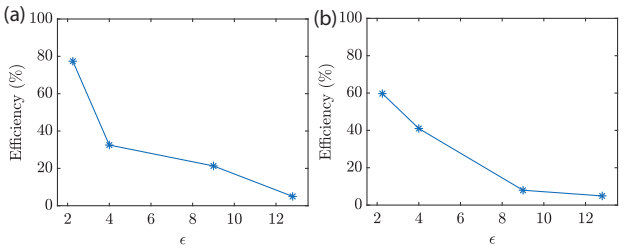

Fig. 14. Focusing efficiencies as a function of the permittivity ϵ of the nanocylinders for photonic patches with (a) initial GA Vogel spiral geometry and (b) initial periodic array geometry. The focusing position is $x_f = 15$ μm, $y_f = 0$, and the wavelength is $\lambda = 1$ μm.

investigated how the performance of the proposed photonic patches scales with the overall footprint of the scattering array. Specifically, we varied the number of nanocylinders N designated in beam shaping and focusing patches and then simulated their corresponding far-field steering or focusing efficiencies. Figure 15(a) shows the results of the differential scattering efficiency of the optimized photonic patches at different wavelengths $\lambda_1 = 1.0$ μm, $\lambda_2 = 1.1$ μm, $\lambda_3 = 1.2$ μm, $\lambda_4 = 1.3$ μm versus N. From Fig. 15(a), it is clear that when N increases, the differential scattering efficiency at each wavelength first increases and then reaches a plateau after a critical number of cylinders, for both the GA Vogel spirals (shown by the solid lines) and the periodic structures (shown by the dashed lines) and for all the investigated wavelengths (labeled by different colors). Figure 15(b) shows the focusing efficiencies at $x_f = 15$ μm with incident wavelength $\lambda = 1$ μm versus N, for both optimized GA Vogel spiral and periodic structures. Consistent with the behavior shown in Fig. 15(a), our results also show that the focusing efficiencies of the optimized patches saturate beyond a critical number of cylinders for both periodic and aperiodic structures. It is also interesting to observe that the optimal focusing efficiencies obtained by optimizing the GA Vogel spiral structures are consistently larger than the ones of the optimized periodic arrays.

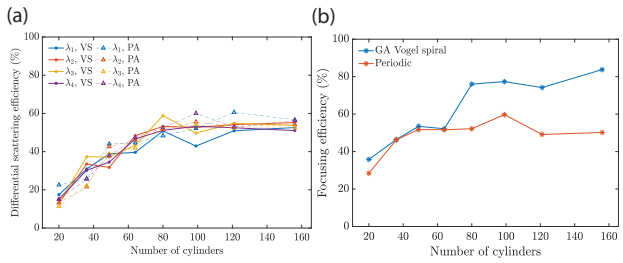

Fig. 15. (a) Differential scattering efficiencies for each wavelength (color labeled in the legend) versus the number of cylinders in the photonics patches with initial GA Vogel spiral geometry (labeled as GA) and initial periodic array geometry (labeled as PA) geometries. (b) Focusing efficiencies of the optimized GA Vogel spirals (blue) and optimized periodic arrays (red).

E. Inverse Design of Photonic Patches for LDOS Enhancement

We now address the enhancement of the LDOS in optimized GA aperiodic photonic patches through adjoint optimization. Depending on the orientation of the excitation dipole, the Purcell enhancement depends only on the $\mathrm{Im}\{G_{zz}\}$, for TM polarization, or on the $\mathrm{Im}\{G_{xx}+G_{yy}\}$, for TE polarization. Therefore, we introduced

$$g_{\mathrm{TE}} = \mathrm{Im}\{G_{xx}+G_{yy}\}, \tag{65}$$

an objective function to maximize the TE Purcell enhancement. For the TM Purcell enhancement we used

$$g_{\mathrm{TM}} = \mathrm{Im}\{G_{zz}\}, \tag{66}$$

where the expressions for G_{xx}, G_{yy}, and G_{zz} were given in Eqs. (41)–(43). The derivative $g_{\mathbf{b}}'$ can be readily obtained from

$$\frac{\partial(\mathrm{Im}\,G_{xx})}{\partial \hat{b}_{n\ell}} = b_{n\ell}e^{j\ell\theta_{ns}}\left[H_\ell'(k_oR_{ns})\sin(\theta_{ns}) + \frac{j\ell}{k_oR_{ns}}H_\ell(k_oR_{ns})\cos(\theta_{ns})\right], \tag{67}$$

$$\frac{\partial(\mathrm{Im}\,G_{yy})}{\partial \hat{b}_{n\ell}} = -b_{n\ell}e^{j\ell\theta_{ns}}\left[H_\ell'(k_oR_{ns})\cos(\theta_{ns}) - \frac{j\ell}{k_oR_{ns}}H_\ell(k_oR_{ns})\sin(\theta_{ns})\right], \tag{68}$$

$$\frac{\partial(\mathrm{Im}\,G_{zz})}{\partial \hat{b}_{n\ell}} = -jJ_\ell(k_or_n)H_\ell(k_oR_{ns})e^{j\ell\theta_{ns}}. \tag{69}$$

As a relevant example of LDOS enhancement in small-sized photonic patches, we first consider the optimization of the Purcell factor for arrays of dielectric cylinders arranged initially in the GA Vogel spiral geometry. Figure 16 shows an example related to the optimization of a TE mode of the GA Vogel structure. The initial array consists of a GA Vogel spiral with only 50 air holes of initial radii $r = 200$ nm and an averaged center-to-center particle distance $d_1 = 0.50$ μm. Note that the cylinders here consist of air holes embedded in a dielectric medium with $\epsilon_o = 12.8$, since in this configuration a TE-polarized bandgap is expected to open for relatively small-sized arrays, hosting high-quality factor band-edge modes [16,17,23]. In particular, the analyzed structure supports a strong band-edge resonance excited by a dipole with in-plane orientation for $d_1/\lambda = 0.202363$. The excitation dipole is located at position $(x_s, y_s) = (0.4\ \mu\mathrm{m}, 0.02\ \mu\mathrm{m})$ and we maximize the TE Purcell enhancement at this band-edge resonance by adjusting all the radii and positions of the cylinders in the array. In our computation, we selected a learning rate to update the radii equal to 0.1 while the one used for updating the positions was set equal to 0.001. We then optimized the array using 20,000 iterations. Figure 16(a) compares the Purcell enhancement spectrum for both the initial and the optimized geometry of the array. The black arrow in the panel indicates the spectral position of the targeted band-edge mode. Figure 16(b) clearly illustrates the significant enhancement achieved for the Purcell factor of the considered resonant mode. Moreover, the Purcell enhancements for the initial and the optimized arrays are found to be $F_i \approx 3.58$ and $F_o \approx 10.5$, resulting in an increase by a factor of around three due to the reduced mode volume of the optimized resonance. We further characterized the optical resonant modes by solving the homogeneous T-matrix equation $\mathbf{Tb} = 0$. The resonant modes are obtained by finding the complex eigenvalues $k = \mathrm{Re}(k) + j\,\mathrm{Im}(k)$ that satisfy the relation $\det[\mathbf{T}(k)] = 0$ [9,23]. Here, $\mathrm{Re}(k)$ is equal to the wavenumber of the mode, while $\mathrm{Im}(k)$ corresponds to its decay rate, which is inversely proportional to the spectral width of the mode. We evaluated the resonant modes by generating a 2D map of $\det[\mathbf{T}(k)]$ with a resolution of $\Delta[\mathrm{Re}(k)] = 1.25 \times 10^{-4}\ \mu\mathrm{m}^{-1}$ and $\Delta[\log_{10}\mathrm{Im}(k)] = 0.05$ [23]. The corresponding quality factors are computed according to $Q = |\mathrm{Re}(k)/[2\,\mathrm{Im}(k)]|$ [9,23]. We found that the quality factors for the initial GA Vogel spiral and for the optimized photonic patch are $Q_i \approx 177$ and $Q_o \approx 384$, respectively. Figures 16(c) and 16(d) show the spatial distributions of the Purcell factors (i.e., LDOS maps) of the initial and optimized structures, computed by using a square grid of excitation dipoles with a spacing of 3 nm, oriented in the $\hat{\mathbf{x}}$ and $\hat{\mathbf{y}}$ directions [23]. Figures 16(e) and 16(f) show the spatial distributions of the electric fields of the optical resonances (normalized to their maximum values) corresponding to, respectively, the initial and optimized structures.

To demonstrate the robustness of our design method, we additionally present the optimization of the TM-polarized modes in arrays of dielectric rods with large refractive index contrast [16,17]. Specifically, for the initial configuration we chose the same GA Vogel spiral geometry discussed above but considered 50 dielectric cylinders with large permittivity $\epsilon_n = 12.8$ embedded in air. The spatial and spectral localization properties of the band-edge modes of GA Vogel spiral structures have been intensively investigated in nanophotonics as a viable approach to enable enhanced light–matter interactions over multiple-length scales [52–56]. We chose the location of the excitation dipole at $(x_s, y_s) = (0.0587\ \mu\mathrm{m}, 0.0352\ \mu\mathrm{m})$ to evaluate the TM Purcell enhancement. The learning rates used and the number of iterations were kept the same as in the previously discussed TE case. Figure 17(a) displays in logarithmic scale the spectra of the Purcell factors for the initial and the optimized configurations at the spectral parameter $d_1/\lambda = 0.645193$, indicated by the black arrow. In Fig. 17(b), we compared the spectra of the Purcell factors of the initial and the optimal photonic

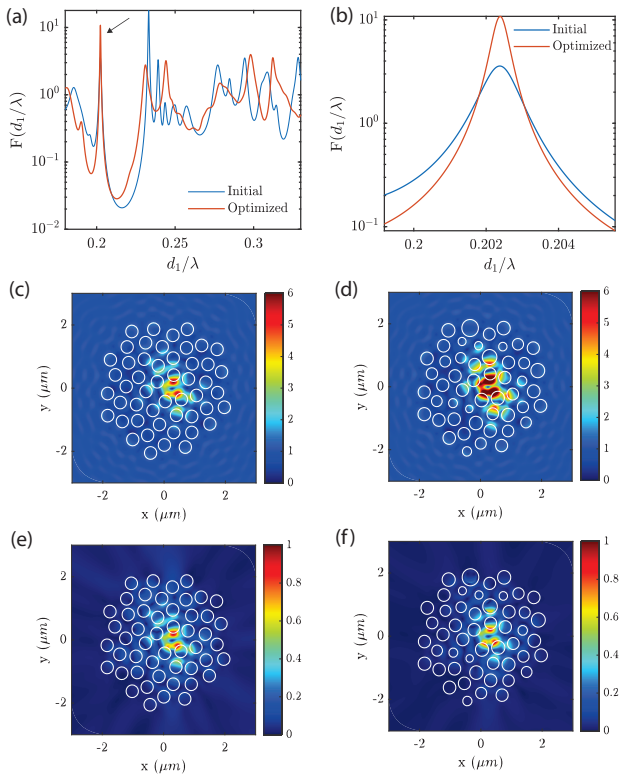

Fig. 16. (a) Purcell factor spectrum for both the initial (blue) and optimized (red) GA Vogel spiral air-hole array with a TE-polarized dipole placed at (0.4 μm, 0.02 μm). The black arrow indicates the spectral parameter $d_1/\lambda = 0.202363$ where we performed adjoint optimization. (b) Purcell factor spectrum for the initial (blue) and optimized (red) photonic patch near the optimized mode. Spatial map of Purcell factors of (c) initial and (d) optimized photonic patches at $d_1/\lambda = 0.202363$. Also shown are the spatial distributions of TE-polarized optical modes for the (e) initial and (f) optimized photonic patches, respectively.

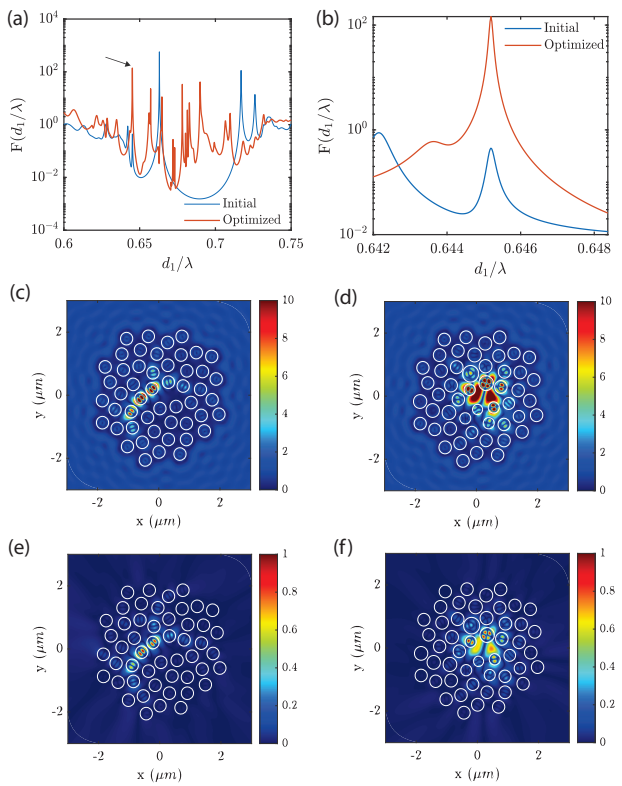

Fig. 17. (a) Purcell factor spectrum for both the initial (blue) and optimized (red) GA Vogel spiral nanocylinder array with TM polarized dipole placed at (0.0587 μm, 0.0352 μm). The black arrow indicates the spectral parameter $d_1/\lambda = 0.645193$ where we performed adjoint optimization. (b) Purcell factor spectrum for the initial (blue) and optimized (red) photonic patch near the optimized mode. Spatial map of Purcell factors of (c) initial and (d) optimized photonic patches at $d_1/\lambda = 0.645193$. Also shown are the spatial distributions of TM-polarized optical modes at $d_1/\lambda = 0.645193$ for the (e) initial and (f) optimized photonic patches, respectively.

patch configurations in a spectral region around the targeted mode. Our results show that the peak value for the initial array is $F_i \approx 0.447$ while the one of the optimized array is $F_o \approx 145$, demonstrating a 324× enhancement. Moreover, we obtained $Q_i \approx 2944$ and $Q_o \approx 6435$ for the initial and for the optimized photonic patches. Figures 17(c) and 17(d) also show the LDOS maps of, respectively, the initial and optimized structures, excited by a grid of $\hat{\mathbf{z}}$-oriented dipoles with the same spacing as the TE-polarized case. Finally, Figs. 17(e) and 17(f) display the spatial distributions of the resonant modes for, respectively, the initial and optimized structures. For a more complete study of the LDOS enhancement, we also investigated the performance of the adjoint optimization on the most localized band-edge mode of the initial GA Vogel spiral. Fig. 18(a) shows the spectra of Purcell factors for the initial and the optimized structures at $d_1/\lambda = 0.645193$, and we display the effect of the Purcell factor optimization over a smaller spectral region around the selected mode in Fig. 18(b). Our results show that the optimization improvement for this mode is very modest, with the Purcell factor increasing from $F_i \approx 576$ to $F_o \approx 647$. Therefore, we have established that the Vogel spiral photonic patches already support a strongly localized band-edge mode with an almost

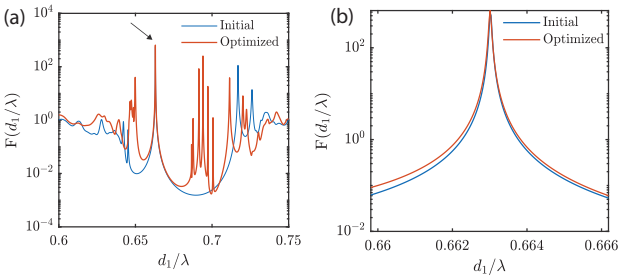

Fig. 18. (a) Purcell factor spectrum for both the initial (blue) and optimized (red) GA Vogel spiral nanocylinder array with TM polarized dipole placed at (0.0587 μm, 0.0352 μm). The black arrow indicates the spectral parameter $d_1/\lambda = 0.660311$ where we performed adjoint optimization. (b) Purcell factor spectrum for the initial (blue) and optimized (red) photonic patch near the targeted mode.

optimal Purcell factor $F \approx Q/V$, where V is defined as the volume of the mode, which is consistent with our previous studies [18,19,35].

To further explore the capabilities of our inverse design approach we investigated the possibility to enhance the LDOS of photonic patches at multiple wavelengths. Similar to the

situation of broadband focusing discussed in Subsection 2.C., we introduced a multi-objective function for the optimization of the Purcell factor at multiple wavelengths as

$$g_{TM} = \sum_{i=1}^{m} g_{TM}(\lambda_i) + \sum_{i \neq j} \left[F(\mathbf{r}; \lambda_i) - F(\mathbf{r}; \lambda_j) \right]^2, \quad \textbf{(70)}$$

where m is the number of considered wavelengths and the cross-difference penalty term is used to minimize the discrepancy between the Purcell factors at different wavelengths. We chose the same initial array and dipole excitation conditions as in the optimization of the TM-polarized single mode discussed before. Additionally, all the learning rate parameters are identical to the previous case but, given the more challenging nature of this problem, we ran the optimization algorithm for 70,000 iterations. Figure 19(a) shows the spectrum of the Purcell enhancement factor obtained when optimizing at the two spectral parameter values $d_1/\lambda = 0.645183, 0.726096$ indicated by the black arrows. The enhancement achieved at both the corresponding wavelengths is directly evident in Figs. 19(b) and 19(c). In particular, at $d_1/\lambda = 0.645183$, the Purcell factor was increased from $F_i \approx 0.441$ to $F_o \approx 199$, which corresponds to a 451× enhancement. The corresponding quality factor was improved from $Q_i \approx 2944$ to $Q_o \approx 3431$. On the other hand, in Fig. 19(c), the Purcell factor at $d_1/\lambda = 0.726096$ was increased from $F_i \approx 13.8$ to $F_o \approx 64.7$, achieving an overall LDOS enhancement by a factor of 4.68. The corresponding quality factor was enhanced from $Q_i \approx 1250$ to $Q_o \approx 2689$. Figures 19(e)–19(g) display the spatial distributions of the LDOS maps at these two spectral parameters, respectively, while Figs. 19(i)–19(k) illustrate the corresponding optical modes. Note that a similar optimization can also be applied to the TE-polarized mode.

Notice that after the optimization, resonant modes start to emerge inside the optical bandgap of the initial GA Vogel spiral structure. As an instance, we investigated a resonant mode located at $d_1/\lambda = 0.683439$, which is indicated by the red arrow in Fig. 19(a). Figure 19(d) indicates the optimized Purcell factor with $F_o \approx 132$. The corresponding quality factor is $Q_o \approx 1.66 \times 10^4$. Figures 19(h) and 19(l) show, respectively, the LDOS maps and the resonant modes excited at $d_1/\lambda = 0.683439$.

Finally, in Fig. 20(a), we optimized the Purcell factor at two frequencies (i.e., at the corresponding spectral parameters indicated by the black arrows) that fall within the bandgap of the initial Vogel spiral structure. Specifically, the selected spectral parameters are $d_1/\lambda = 0.678138$ and $d_1/\lambda = 0.702267$, and we considered 70,000 iterations of our optimization algorithm. Figures 20(b) and 20(c) show that optimized Purcell factors at $d_1/\lambda = 0.645183$ and $d_1/\lambda = 0.726096$, where we obtained $F_o \approx 126$ and $F_o \approx 40.6$, respectively. Their corresponding optimized quality factors are $Q_o \approx 6535$ to $Q_o \approx 4807$. The LDOS maps of the optimized structures at $d_1/\lambda = 0.645183$ and $d_1/\lambda = 0.726096$ are illustrated, respectively, in Figs. 20(d) and 20(e). Figures 20(f) and 20(g) display the selected optical modes for the optimized structures at the same two spectral parameters.

To conclude our study, in Fig. 21(a) we analyzed scaling the ratio between the optimized Purcell factor and initial Purcell

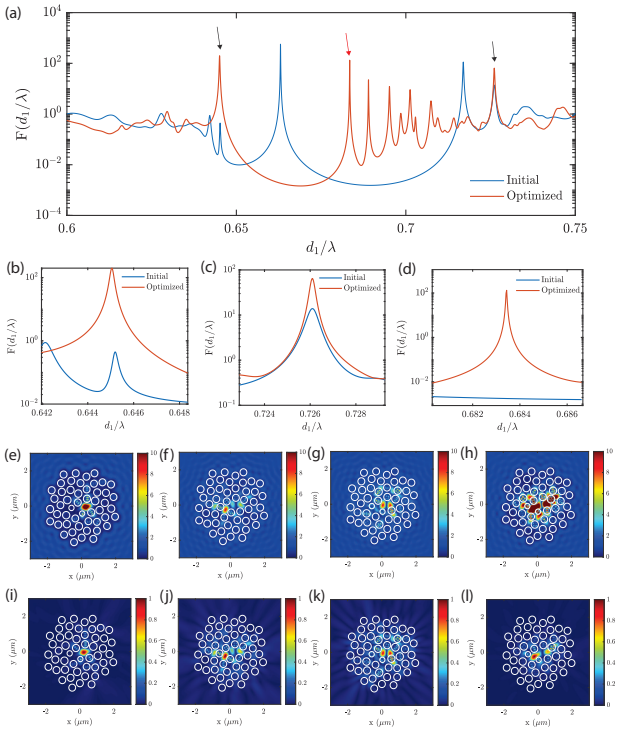

Fig. 19. (a) Purcell factor spectrum for both the initial (blue) and optimized (red) GA Vogel spiral nanocylinder array with TM polarized dipole placed at (0.0587 μm, 0.0352 μm). The two black arrows indicate the specified spectral parameters $d_1/\lambda = 0.645183, 0.726096$ where we performed adjoint optimization. Purcell factor spectrum for the initial (blue) and optimized (red) photonic patch in the spectral regions around (b) $d_1/\lambda = 0.645183$, (c) $d_1/\lambda = 0.726096$, and (d) $d_1/\lambda = 0.683439$ [indicated by red arrow in (a)]. LDOS maps of (e) the optimized structure at $d_1/\lambda = 0.645183$, (f) the initial and (g) the optimized structures at $d_1/\lambda = 0.726096$, and (h) the optimized structure at $d_1/\lambda = 0.683439$. (i)–(l) Spatial distributions of TM-polarized optical resonant modes, corresponding to the conditions in (e)–(h), respectively.

factor F_o/F_i as a function of the number of cylinders N in the photonic patch. To perform this analysis, we considered the same modes and structure optimized in this subsection. Specifically, we investigated the optimization performance of the TM modes at $d_1/\lambda = 0.645193$ [as in Fig. 17(b)], $d_1/\lambda = 0.726096$ [as in Fig. 19(c)], and the TE mode at $d_1/\lambda = 0.202363$ [as in Fig. 16(b)] for structures with different N. In these configurations, the optimized modes are strongly localized in a small area at the center of the photonic patch. Consistently, due to the initial decrease of the optimized mode volume, we found that the ratio $F_o/F_i \approx (Q_o V_i)/(Q_i V_o)$ features a peak for photonic patches with an optimal size, which depends on the spectral parameter d_1/λ of the mode. Beyond this point, the optimization enhancement decreases because the size of the photonic patch exceeds the characteristic localization length of the considered mode. Figure 21(b) displays the enhancement of the ratios of the corresponding quality factors Q_o/Q_i. In the case of the optimized TM mode at $d_1/\lambda = 0.645193$ (blue curve), we observed a decreasing trend with respect to the number of cylinders N. As N increases, we found that Q_o/Q_i decreases and converges to unity when the photonic patches have ≈ 100 cylinders. For the optimized

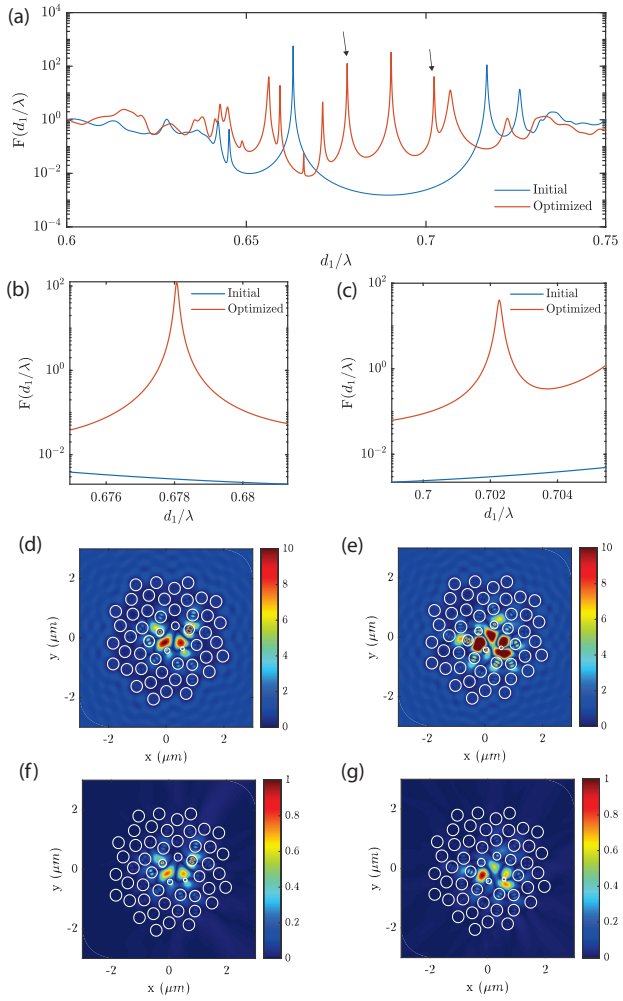

Fig. 20. (a) Purcell factor spectrum for both the initial (blue) and optimized (red) GA Vogel spiral nanocylinder array with a TM-polarized dipole placed at (0.0587 μm, 0.0352 μm). The two black arrows indicate the specified spectral parameters $d_1/\lambda = 0.678138$, 0.702267 where we performed adjoint optimization. Purcell factor spectrum for the initial (blue) and optimized (red) photonic patch in the spectral regions around (b) $d_1/\lambda = 0.678138$ and (c) $d_1/\lambda = 0.702267$. Optimized LDOS maps at (d) $d_1/\lambda = 0.678138$ and (e) $d_1/\lambda = 0.702267$. Also shown are the spatial distributions of TM-polarized optical modes at (f) $d_1/\lambda = 0.678138$ and (g) $d_1/\lambda = 0.702267$, respectively.

TM mode at $d_1/\lambda = 0.726096$ (red curve), the quality factor ratio decreases at first and then increases until it reaches a nearly constant value, as N increases. As for the TE mode at $d_1/\lambda = 0.202363$ (yellow curve), we noticed that the ratio generally increases as N increases. This behavior can be explained by the fact that we are considering the properties of a resonant mode that is strongly localized in the central region of the photonic patch, as shown in Fig. 17(d). In fact, this mode is characterized by a small localization length ℓ_{loc} on the order of only a few cylinders [16,24,35]. Therefore, depending on the value of ℓ_{loc}, a critical size for the photonic patch exists, beyond which the benefits of mode optimization are essentially lost. Since $F \approx Q/V$, where V is the mode volume, this occurs when the size of the device exceeds the characteristic localization

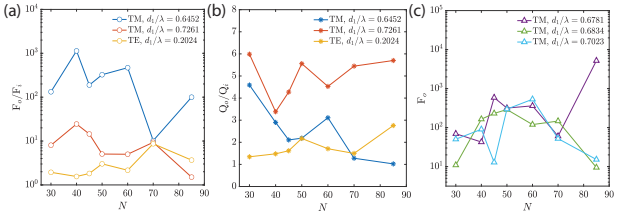

Fig. 21. (a) Purcell factor enhancement F_o/F_i in semilog scale and (b) quality factor enhancement Q_o/Q_i with respect to number of scatterers N, for TM modes at $d_1/\lambda = 0.645183$, 0.726096 and TE mode at $d_1/\lambda = 0.202363$. (c) Purcell factor after optimization F_o in semilog scale with respect to number of scatterers N, for TM modes at $d_1/\lambda = 0.678138$, 0.683439, and 0.702267.

length of the considered mode. Under these circumstances, the localized modes decouple from the rest of the structure, consistent with Fig. 21(a). On the other hand, we established that the most effective region of optimization with respect to N varies from mode to mode, as shown in Fig. 21(b). Finally, we presented the scaling analysis of mode optimization inside the bandgap. Particularly, we investigated the TM modes at $d_1/\lambda = 0.678138$, 0.683439, and 0.702267, which correspond to Fig. 20(b), Fig. 19(d), and Fig. 20(c). Since there are no localized modes inside the bandgap of the initial GA Vogel spiral patches, their initial Purcell factors cannot be defined in this case. Hence, we only showed the Purcell factors of the optimized structures in Fig. 21(c). As F_o changes with N, notice that the curves feature optimal regions that are consistent with Fig. 21(a) with respect to the given sizes of photonic patches, depending on the chosen spectral parameters of the modes.

3. CONCLUSIONS

In this paper, we proposed and demonstrated a robust photonic inverse design method by combining adjoint optimization with rigorous semi-analytical 2D-GMT. We reviewed the GMT formalism in detail and derived closed-form analytical expressions that enabled the efficient application of the gradient-based adjoint optimization of far-field and near-field relevant properties of photonic patches. We focused on multiwavelength radiation shaping, near-field focusing, and the enhancement of the local density of states. Specifically, we demonstrated efficient far-field radiation shaping at multiple wavelengths in photonic patches optimized starting from both periodic and Vogel spiral configurations, achieving a differential scattering efficiency of approximately 60%. In addition, we designed compact focusing structures using both optimized aperiodic and periodic patches that enhanced the field intensity at specified locations in the Fresnel zone with focusing efficiencies in excess of 75%. We also demonstrated improved broadband focusing performances in optimized GA Vogel spiral patches. Finally, we presented the design of optimized patches that enhance the LDOS and mode localization with both TE- and TM-polarized excitations at multiple wavelengths. We finally investigated the scaling of the optimized performances of photonic patches of different sizes. The combination of the semi-analytical 2D-GMT method with the adjoint optimization algorithm provides a robust inverse design methodology to develop compact photonic devices with optimal functionalities. Without the need for spatial meshing,

we believe the developed approach provides efficient multiple scattering solutions with a strongly reduced computational burden compared to standard numerical simulation techniques and enables novel, more compact geometries for on-chip photonics and metamaterials device technologies.

APPENDIX A: DERIVATIVE OF THE TRANSFER MATRIX

$$\begin{aligned}\frac{\partial \hat{\mathbf{T}}_{nn'}^{\ell\ell'}}{\partial p_i} = &-(1-\delta_{nn'})\, e^{j(\ell'-\ell)\phi_{nn'}}\Bigg[j(\ell'-\ell)\, H_{\ell-\ell'}(k_o R_{nn'})\, s_{n\ell} \\ &\times \frac{J_{\ell'}(k_o r_{n'})}{J_\ell(k_o r_n)} \frac{\partial \phi_{nn'}}{\partial p_i} + k_o\, H'_{\ell-\ell'}(k_o R_{nn'})\, s_{n\ell} \frac{J_{\ell'}(k_o r_{n'})}{J_\ell(k_o r_n)} \\ &\times \frac{\partial R_{nn'}}{\partial p_i} + H_{\ell-\ell'}(k_o R_{nn'}) \frac{J_{\ell'}(k_o r_{n'})}{J_\ell(k_o r_n)} \frac{\partial s_{n\ell}}{\partial p_i} \\ &+ k_o\, H_{\ell-\ell'}(k_o R_{nn'})\, s_{n\ell} \frac{J'_{\ell'}(k_o r_{n'})}{J_\ell(k_o r_n)} \frac{\partial r_{n'}}{\partial p_i} \\ &- k_o\, H_{\ell-\ell'}(k_o R_{nn'})\, s_{n\ell} \frac{J_{\ell'}(k_o r_{n'})}{J_\ell(k_o r_n)^2} J'_\ell(k_o r_n) \frac{\partial r_n}{\partial p_i}\Bigg],\end{aligned} \tag{A1}$$

where the derivatives of $s_{n\ell}$ and $\Gamma_{n\ell}$ are

$$\begin{aligned}\frac{\partial s_{n\ell}}{\partial p_i} = &-\Bigg[k_o J''_\ell(k_o r_n) \frac{\partial r_n}{\partial p_i} - \frac{\partial \Gamma_{n\ell}}{\partial p_i} J_\ell(k_o r_n) \\ &- k_o \Gamma_{n\ell} \frac{\partial r_n}{\partial p_i} J'_\ell(k_o r_n)\Bigg] \Big/ \left[H'_\ell(k_o r_n) - \Gamma_{n\ell} H_\ell(k_o r_n)\right] \\ &+ \Bigg[k_o H''_\ell(k_o r_n) \frac{\partial r_n}{\partial p_i} - \frac{\partial \Gamma_{n\ell}}{\partial p_i} H_\ell(k_o r_n) - k_o \Gamma_{n\ell} \frac{\partial r_n}{\partial p_i} \\ &\times H'_\ell(k_o r_n)\Bigg] \Big/ \frac{\left(H'_\ell(k_o r_n) - \Gamma_{n\ell} H_\ell(k_o r_n)\right)^2}{J'_\ell(k_o r_n) - \Gamma_{n\ell} J_\ell(k_o r_n)},\end{aligned} \tag{A2}$$

$$\frac{\partial \Gamma_{n\ell}}{\partial p_i} = \xi_n \frac{k_n^2}{k_o} \frac{\partial r_n}{\partial p_i} \left[\frac{J''_\ell(k_n r_n)}{J_\ell(k_n r_n)} - \frac{J'_\ell(k_n r_n)^2}{J_\ell(k_n r_n)^2}\right]. \tag{A3}$$

The derivatives of $R_{nn'}$, $\phi_{nn'}$ with respect to the different geometrical parameters can be found in Table 2.

APPENDIX B: DERIVATIVE OF THE PLANE WAVE EXCITATION COEFFICIENTS

For a plane wave propagating at an angle Θ with respect to the $+\hat{x}$ in the 2D geometry, the coefficient $\hat{\mathbf{a}}^0$ is given by [9]

$$\hat{a}_{n\ell}^{0E} = \frac{a_{n\ell}^{0E}}{J_\ell(k_o r_n)} = \frac{j^l e^{j\mathbf{k}_o\cdot\mathbf{R}_n} e^{-j\ell\Theta}}{J_\ell(k_o r_n)}, \tag{B1}$$

Table 2. Derivatives of Relative Cylinder Positions with Respect to Design Parameters

$\frac{\partial R_{nn'}}{\partial x_j} = \frac{x_n - x_{n'}}{R_{nn'}}(\delta_{jn} + \delta_{jn'})$	$\frac{\partial \phi_{nn'}}{\partial x_j} = \frac{\sin(\phi_{nn'})}{R_{nn'}}(\delta_{jn'} - \delta_{jn})$
$\frac{\partial R_{nn'}}{\partial y_j} = \frac{y n_n - y_{n'}}{R_{nn'}}(\delta_{jn} + \delta_{jn'})$	$\frac{\partial \phi_{nn'}}{\partial y_j} = \frac{\cos(\phi_{nn'})}{R_{nn'}}(\delta_{jn'} - \delta_{jn})$
$\frac{\partial R_{nn'}}{\partial r_j} = 0$	$\frac{\partial \phi_{nn'}}{\partial r_j} = 0$

where $\mathbf{k}_o = k_o \cos(\Theta)\hat{\mathbf{x}} + k_o \sin(\Theta)\hat{\mathbf{y}}$ is the wavenumber in the host medium and $\mathbf{R}_n = (x_n, y_n)$ is the position of the nth cylinder. The derivatives of the source expansion coefficients are given by

$$\frac{\partial \hat{\mathbf{a}}^0}{\partial p_i} = \frac{a_{n\ell}^{0E}}{J_\ell(k_o r_n)} \left[j s_{n\ell} \mathbf{k}_o \cdot \frac{\partial \mathbf{R}_n}{\partial p_i} + \frac{\partial s_{n\ell}}{\partial p_i} - s_{n\ell} k_o \frac{J'_\ell(k_o r_n)}{J_\ell(k_o r_n)} \frac{\partial r_n}{\partial p_i}\right], \tag{B2}$$

where the partial derivative of $s_{n\ell}$ is given in Eq. (A2) and the partial derivatives of r_n are given in Table 1.

APPENDIX C: DERIVATIVE OF THE DIPOLE EXCITATION COEFFICIENTS

The source coefficients $\hat{\mathbf{a}}^0$ for a dipole in the host medium with different orientations are [28]

$$a_{n\ell,x}^{0E} = -\frac{1}{8j}\left[H_{\ell+1}(k_o R_{ns}) e^{-j(\ell+1)\theta_{ns}} + H_{\ell-1}(k_o R_{ns}) e^{-j(\ell-1)\theta_{ns}}\right], \tag{C1}$$

$$a_{n\ell,y}^{0E} = -\frac{1}{8}\left[H_{\ell+1}(k_o R_{ns}) e^{-j(\ell+1)\theta_{ns}} - H_{\ell-1}(k_o R_{ns}) e^{-j(\ell-1)\theta_{ns}}\right], \tag{C2}$$

$$a_{n\ell,z}^{0E} = \frac{1}{4j} H_\ell(k_o R_{ns}) e^{-j\ell\theta_{ns}}, \tag{C3}$$

where $(R_{\text{is}}, \theta_{\text{is}})$ are the polar coordinates of the source positions (x_s, y_s) in the frame of reference of the ith cylinder center. The subscripts x, y, z indicate the dipole orientation.

Therefore, the derivatives of $\hat{\mathbf{a}}^0$ for the exterior dipole sources along different orientations are computed as

$$\begin{aligned}\frac{\partial \hat{\mathbf{a}}_x^0}{\partial p_i} = &\hat{a}_{n\ell,x}^{0E}\left[\frac{1}{s_{n\ell}} \frac{\partial s_{n\ell}}{\partial p_i} - k_o \frac{J'_\ell(k_o r_n)}{J_\ell(k_o r_n)} \frac{\partial r_n}{\partial p_i}\right] - \frac{1}{8j} e^{-j(\ell+1)\theta_{ns}} \\ &\times \left(k_o H'_{\ell+1}(k_o R_{ns}) \frac{\partial R_{ns}}{\partial p_i} - j(\ell+1) H_{\ell+1}(k_o R_{ns}) \frac{\partial \theta_{ns}}{\partial p_i}\right) \\ &- \frac{1}{8j} e^{-j(\ell-1)\theta_{ns}} \Bigg(k_o H'_{\ell-1}(k_o R_{ns}) \frac{\partial R_{ns}}{\partial p_i} - j(\ell-1) \\ &\times H_{\ell-1}(k_o R_{ns}) \frac{\partial \theta_{ns}}{\partial p_i}\Bigg),\end{aligned} \tag{C4}$$

$$\begin{aligned}\frac{\partial \hat{\mathbf{a}}_y^0}{\partial p_i} = &\hat{a}_{n\ell,y}^{0E}\left[\frac{1}{s_{n\ell}} \frac{\partial s_{n\ell}}{\partial p_i} - k_o \frac{J'_\ell(k_o r_n)}{J_\ell(k_o r_n)} \frac{\partial r_n}{\partial p_i}\right] - \frac{1}{8} e^{-j(\ell+1)\theta_{ns}} \\ &\times \left(k_o H'_{\ell+1}(k_o R_{ns}) \frac{\partial R_{ns}}{\partial p_i} - j(\ell+1) H_{\ell+1}(k_o R_{ns}) \frac{\partial \theta_{ns}}{\partial p_i}\right) \\ &+ \frac{1}{8} e^{-j(\ell-1)\theta_{ns}} \Bigg(k_o H'_{\ell-1}(k_o R_{ns}) \frac{\partial R_{ns}}{\partial p_i} - j(\ell-1) \\ &\times H_{\ell-1}(k_o R_{ns}) \frac{\partial \theta_{ns}}{\partial p_i}\Bigg),\end{aligned} \tag{C5}$$

Table 3. Derivatives of Relative Cylinder Positions with Respect to Design Parameters

$\frac{\partial R_{ns}}{\partial x_i} = -\cos(\theta_{ns})\delta_{in}$	$\frac{\partial \theta_{ns}}{\partial x_i} = +\frac{\sin(\theta_{ns})}{R_{ns}}\delta_{in}$
$\frac{\partial R_{ns}}{\partial y_i} = -\sin(\theta_{ns})\delta_{in}$	$\frac{\partial \theta_{ns}}{\partial y_i} = -\frac{\cos(\theta_{ns})}{R_{ns}}\delta_{in}$
$\frac{\partial R_{ns}}{\partial r_i} = 0$	$\frac{\partial \theta_{ns}}{\partial r_i} = 0$

$$\frac{\partial \hat{\mathbf{a}}_z^0}{\partial p_i} = \hat{a}_{n\ell,z}^{0E}\left[\frac{1}{s_{n\ell}}\frac{\partial s_{n\ell}}{\partial p_i} - k_o\frac{J_\ell'(k_o r_n)}{J_\ell(k_o r_n)}\frac{\partial r_n}{\partial p_i}\right] + \frac{1}{4j}e^{-j\ell\theta_{ns}} \times\left[k_o H_\ell'(k_o R_{ns})\frac{\partial R_{ns}}{\partial p_i} - j\ell H_\ell(k_o R_{ns})\frac{\partial \theta_{ns}}{\partial p_i}\right], \tag{C6}$$

where the derivative of R_{ns}, θ_{ns} with respect to the design parameters can be found in Table 3.

Funding. Army Research Office (W911NF2210110); National Science Foundation (ECCS-2015700, ECCS-2110204).

Acknowledgment. The authors wish to acknowledge the support of the author community in using REVTeX, offering suggestions and encouragement, and testing new versions. We would also like to thank Prof. Alejandro Rodriguez from Princeton University for insightful discussions on the adjoint optimization of photonic structures.

Disclosures. The authors declare no conflicts of interest.

Data availability. The data that support the findings of this study are available from the corresponding author upon reasonable request.

REFERENCES

1. S. Molesky, Z. Lin, A. Y. Piggott, W. Jin, J. Vucković, and A. W. Rodriguez, "Inverse design in nanophotonics," Nat. Photonics **12**, 659–670 (2018).
2. S. Ruder, "An overview of gradient descent optimization algorithms," arXiv, arXiv:1609.04747 (2016).
3. D. Sell, J. Yang, S. Doshay, R. Yang, and J. A. Fan, "Large-angle, multifunctional metagratings based on freeform multimode geometries," Nano Lett. **17**, 3752–3757 (2017).
4. F. Callewaert, V. Velev, P. Kumar, A. Sahakian, and K. Aydin, "Inverse-designed broadband all-dielectric electromagnetic metadevices," Sci. Rep. **8**, 1358 (2018).
5. M. Mansouree, A. McClung, S. Samudrala, and A. Arbabi, "Large-scale parametrized metasurface design using adjoint optimization," ACS Photon. **8**, 455–463 (2021).
6. A. Y. Piggott, J. Lu, K. G. Lagoudakis, J. Petykiewicz, T. M. Babinec, and J. Vučković, "Inverse design and demonstration of a compact and broadband on-chip wavelength demultiplexer," Nat. Photonics **9**, 374–377 (2015).
7. L. Su, A. Y. Piggott, N. V. Sapra, J. Petykiewicz, and J. Vučković, "Inverse design and demonstration of a compact on-chip narrowband three-channel wavelength demultiplexer," ACS Photon. **5**, 301–305 (2018).
8. T. W. Hughes, M. Minkov, I. A. Williamson, and S. Fan, "Adjoint method and inverse design for nonlinear nanophotonic devices," ACS Photon. **5**, 4781–4787 (2018).
9. D. Gagnon and L. J. Dube, "Lorenz–Mie theory for 2D scattering and resonance calculations," J. Opt. **17**, 103501 (2015).
10. M. Zhou, D. Liu, S. W. Belling, H. Cheng, M. A. Kats, S. Fan, M. L. Povinelli, and Z. Yu, "Inverse design of metasurfaces based on coupled-mode theory and adjoint optimization," ACS Photon. **8**, 2265–2273 (2021).
11. A. Zhan, T. K. Fryett, S. Colburn, and A. Majumdar, "Inverse design of optical elements based on arrays of dielectric spheres," Appl. Opt. **57**, 1437–1446 (2018).
12. M. V. Zhelyeznyakov, A. Zhan, and A. Majumdar, "Design and optimization of ellipsoid scatterer-based metasurfaces via the inverse T-matrix method," OSA Contin. **3**, 89–103 (2020).
13. W. Ma, Z. Liu, Z. A. Kudyshev, A. Boltasseva, W. Cai, and Y. Liu, "Deep learning for the design of photonic structures," Nat. Photonics **15**, 77–90 (2021).
14. S. Colburn and A. Majumdar, "Inverse design and flexible parameterization of meta-optics using algorithmic differentiation," Commun. Phys. **4**, 65 (2021).
15. M. Qiu, "Effective index method for heterostructure-slab-waveguide-based two-dimensional photonic crystals," Appl. Phys. Lett. **81**, 1163–1165 (2002).
16. O. J. Trojak, S. Gorsky, F. Sgrignuoli, F. A. Pinheiro, S.-I. Park, J. D. Song, L. Dal Negro, and L. Sapienza, "Cavity quantum electrodynamics with solid-state emitters in aperiodic nano-photonic Vogel-spiral devices," Appl. Phys. Lett. **117**, 124006 (2020).
17. O. J. Trojak, S. Gorsky, C. Murray, F. Sgrignuoli, F. A. Pinheiro, L. Dal Negro, and L. Sapienza, "Cavity-enhanced light–matter interaction in Vogel-spiral devices as a platform for quantum photonics," Appl. Phys. Lett. **118**, 011103 (2021).
18. F. Sgrignuoli, R. Wang, F. A. Pinheiro, and L. Dal Negro, "Localization of scattering resonances in aperiodic Vogel spirals," Phys. Rev. B **99**, 104202 (2019).
19. S. F. Liew, H. Noh, J. Trevino, L. Dal Negro, and H. Cao, "Localized photonic band edge modes and orbital angular momenta of light in a golden-angle spiral," Opt. Express **19**, 23631–23642 (2011).
20. M. Soljačić and J. D. Joannopoulos, "Enhancement of nonlinear effects using photonic crystals," Nat. Mater. **3**, 211–219 (2004).
21. O. D. Miller, C. W. Hsu, M. H. Reid, W. Qiu, B. G. DeLacy, J. D. Joannopoulos, M. Soljačić, and S. G. Johnson, "Fundamental limits to extinction by metallic nanoparticles," Phys. Rev. Lett. **112**, 123903 (2014).
22. J. Joannopoulos, S. Johnson, J. Winn, and R. Meade, *Photonic Crystals: Molding the Flow of Light*, 2nd ed. (Princeton University, 2008).
23. L. Dal Negro, Y. Chen, S. Gorsky, and F. Sgrignuoli, "Aperiodic bandgap structures for enhanced quantum two-photon sources," J. Opt. Soc. Am. B **38**, C94–C104 (2021).
24. L. Dal Negro, *Waves in Complex Media* (Cambridge University, 2022).
25. P. A. Martin, *Multiple Scattering: Interaction of Time-Harmonic Waves with N Obstacles* (Cambridge University, 2006).
26. A. Z. Elsherbeni and A. A. Kishk, "Modeling of cylindrical objects by circular dielectric and conducting cylinders," IEEE Trans. Antennas Propag. **40**, 96–99 (1992).
27. L. Rayleigh, "XLI. The dispersal of light by a dielectric cylinder," London Edinburgh Dublin Philos. Mag. J. Sci. **36**, 365–376 (1918).
28. A. A. Asatryan, K. Busch, R. C. McPhedran, L. C. Botten, C. M. de Sterke, and N. A. Nicorovici, "Two-dimensional Green tensor and local density of states in finite-sized two-dimensional photonic crystals," Waves Random Media **13**, 9–25 (2003).
29. A. Forouzmand, M. M. Salary, S. Inampudi, and H. Mosallaei, "A tunable multigate indium-tin-oxide-assisted all-dielectric metasurface," Adv. Opt. Mater. **6**, 1701275 (2018).
30. R. Sprik, B. A. van Tiggelen, and A. Lagendijk, "Optical emission in periodic dielectrics," Europhys. Lett. **35**, 265 (1996).
31. L. Novotny and B. Hecht, *Principles of Nano-Optics* (Cambridge University, 2012).
32. R. Balian and C. Bloch, "Distribution of eigenfrequencies for the wave equation in a finite domain. II. Electromagnetic field. Riemannian spaces," Ann. Phys. **64**, 271 (1971).
33. A. Y. Piggott, J. Petykiewicz, L. Su, and J. Vučković, "Fabrication-constrained nanophotonic inverse design," Sci. Rep. **7**, 1786 (2017).
34. J. A. Adam, *A Mathematical Nature Walk* (Princeton University, 2011).
35. J. Trevino, S. F. Liew, H. Noh, H. Cao, and L. Dal Negro, "Geometrical structure, multifractal spectra and localized optical modes of aperiodic Vogel spirals," Opt. Express **20**, 3015–3033 (2012).
36. N. Lawrence, J. Trevino, and L. Dal Negro, "Control of optical orbital angular momentum by Vogel spiral arrays of metallic nanoparticles," Opt. Lett. **37**, 5076–5078 (2012).

37. M. E. Pollard and G. J. Parker, "Low-contrast bandgaps of a planar parabolic spiral lattice," Opt. Lett. **34**, 2805–2807 (2009).
38. J. Trevino, H. Cao, and L. Dal Negro, "Circularly symmetric light scattering from nanoplasmonic spirals," Nano Lett. **11**, 2008–2016 (2011).
39. J. Trevino, C. Forestiere, G. Di Martino, S. Yerci, F. Priolo, and L. Dal Negro, "Plasmonic-photonic arrays with aperiodic spiral order for ultra-thin film solar cells," Opt. Express **20**, A418–A430 (2012).
40. M. Razi, R. Wang, Y. He, R. M. Kirby, and L. Dal Negro, "Optimization of large-scale Vogel spiral arrays of plasmonic nanoparticles," Plasmonics **14**, 253–261 (2019).
41. P. Berini, "Optical beam steering using tunable metasurfaces," ACS Photon. **9**, 2204–2218 (2022).
42. G. K. Shirmanesh, R. Sokhoyan, P. C. Wu, and H. A. Atwater, "Electro-optically tunable multifunctional metasurfaces," ACS Nano **14**, 6912–6920 (2020).
43. A. C. Lesina, D. Goodwill, E. Bernier, L. Ramunno, and P. Berini, "Tunable plasmonic metasurfaces for optical phased arrays," IEEE J. Sel. Top. Quantum Electron. **27**, 4700116 (2021).
44. J. Park, B. G. Jeong, S. I. Kim, *et al.*, "All-solid-state spatial light modulator with independent phase and amplitude control for three-dimensional LiDAR applications," Nat. Nanotechnol. **16**, 69–76 (2021).
45. C. Meng, S. Tang, F. Ding, and S. I. Bozhevolnyi, "Optical gap-surface plasmon metasurfaces for spin-controlled surface plasmon excitation and anomalous beam steering," ACS Photon. **7**, 1849–1856 (2020).
46. P. Sutton, "Introduction to Fourier optics," Quantum Semiclass. Opt. J. Eur. Opt. Soc. Part B **8**, 1095 (1996).
47. I. M. Vellekoop and A. Mosk, "Focusing coherent light through opaque strongly scattering media," Opt. Lett. **32**, 2309–2311 (2007).
48. I. M. Vellekoop, A. Lagendijk, and A. Mosk, "Exploiting disorder for perfect focusing," Nat. Photonics **4**, 320–322 (2010).
49. T. F. Krauss and M. Richard, "Photonic crystals in the optical regime—past, present and future," Prog. Quantum Electron. **23**, 51–96 (1999).
50. C. Wiesmann, K. Bergenek, N. Linder, and U. T. Schwarz, "Photonic crystal LEDs–designing light extraction," Laser Photon. Rev. **3**, 262–286 (2009).
51. N. Lawrence, J. Trevino, and L. Dal Negro, "Aperiodic arrays of active nanopillars for radiation engineering," J. Appl. Phys. **111**, 113101 (2012).
52. R. Wang, F. A. Pinheiro, and L. Dal Negro, "Spectral statistics and scattering resonances of complex primes arrays," Phys. Rev. B **97**, 024202 (2018).
53. F. Sgrignuoli, S. Gorsky, W. A. Britton, R. Zhang, F. Riboli, and L. Dal Negro, "Multifractality of light in photonic arrays based on algebraic number theory," Commun. Phys. **3**, 106 (2020).
54. E. M. Barber, *Aperiodic Structures in Condensed Matter: Fundamentals and Applications* (CRC Press, 2008).
55. L. Dal Negro, *Optics of Aperiodic Structures: Fundamentals and Device Applications* (Pan Stanford, 2013).
56. M. Prado, F. Sgrignuoli, Y. Chen, L. Dal Negro, and F. A. Pinheiro, "Structural entropy and spatial decay of quasimodes in Vogel spirals," Phys. Rev. B **104**, 184204 (2021).